Composite Functional Materials
2026, 2(1): 20260103 https://doi.org/10.63823/20260103

REVIEW ARTICLE

Hot electron back-Injection from plasmonic Au nanoparticles boosts photocatalytic CO_2 reduction over Boron-doped spherical g-C_3N_4

Xianghai Song[a], Huiling Zhao[a], Sheng Xu[a], Xiang Liu[b], Mei Wang[c,*], Xin Liu[a], Weiqiang Zhou[a], Jisheng Zhang[a], Yuanfeng Wu[d], Pengwei Huo[a,*]

a. Institute of Green Chemistry and Chemical Technology, School of Chemistry and Chemical Engineering, Jiangsu University, Zhenjiang 212013, China
b. Jiangsu Higher Vocational College Engineering Research Center of Green Energy and Low Carbon Materials, Zhenjiang College, Zhenjiang 212028, China
c. School of Agricultural Engineering, Jiangsu University, Zhenjiang 212013, China
d. School of Chemistry and Chemical Engineering, Henan Polytechnic University, Jiaozuo 454003, China

ABSTRACT: Converting CO_2 into high-value fuels through the synergistic interplay of donor-acceptor (DA) structure and photothermal effects presents a promising strategy for enhancing the carbon cycle and mitigating greenhouse gas emissions. In this work, a carbon nitride (g-C_3N_4) based photocatalyst, designated Au/BMNS-x, was engineered to integrate both a DA structure and Localized Surface Plasmon Resonance (LSPR) by simultaneously incorporating boron doping and Au nanoparticles (NPs) into g-C_3N_4. The plasmonic Au NPs generate a pronounced photothermal effect under irradiation, significantly elevating the local reaction temperature during CO_2 photoreduction. Real-time infrared thermography demonstrated that Au/BMNS-2 reached a stabilized surface temperature of 148.1°C, which is 1.17 times higher than that of BMNS and 2.06 times greater than pristine g-C_3N_4. Under optimized conditions, Au/BMNS-2 exhibited a CO production rate 5.99 times higher than that of pristine g-C_3N_4, along with excellent structural stability and reusability over multiple cycles. *In situ* X-ray photoelectron spectroscopy (XPS) and femtosecond transient absorption spectroscopy (fs-TAS) provide direct evidence of hot electron back-injection from plasmonic Au NPs into BMNS, enriching electron density around the catalytic active sites. Crucially, the DA structure, synergistically coupled with the LSPR effect, enables highly efficient separation and ultrafast transfer of photogenerated charge carriers, thereby significantly enhancing overall photocatalytic performance. The reaction mechanism was further elucidated through *in situ* Fourier transform infrared spectroscopy (FT-IR) spectroscopy and density functional theory (DFT) simulation. This study offers a rational design strategy for multifunctional photocatalysts that harness both plasmonic and photothermal effects, opening new avenues for high-efficiency solar-driven CO_2 conversion technologies.

KEYWORDS: Photocatalysis, CO_2 reduction, Boron-doping, Au NPs, LSPR

Received: November 5, 2025. **Revised:** January 21, 2026. **Accepted:** March 20, 2026. **Available online:** March 30, 2026
***Corresponding authors:** 1000004927@ujs.edu.cn (Mei Wang); huopw@ujs.edu.cn(Pengwei Huo)

1. Introduction

Photocatalytic technology has emerged as a promising approach for sustainable energy development and environmental remediation, attracting widespread interest in the scientific community [1-3]. Among its various applications, photocatalytic CO_2 reduction stands out as a particularly attractive strategy, as it simultaneously mitigates greenhouse gas emissions and converts CO_2 into valuable solar fuels, offering a dual benefit for addressing climate change and advancing renewable energy storage [4-6]. Among the diverse range of photocatalytic materials, g-C_3N_4 has garnered significant attention due to its favorable electronic band structure, visible-light responsiveness, and excellent chemical and thermal stability [7], making it a promising candidate for CO_2 reduction [8]. However, bulk g-C_3N_4 suffers from several intrinsic limitations that hinder its practical performance. Its layered structure typically results in a low specific surface area and limited exposure of active sites, restricting the adsorption and activation of CO_2 molecules. Moreover, the long migration distance of photogenerated charge carriers and rapid recombination kinetics lead to poor quantum efficiency [9]. These structural and electronic drawbacks collectively impede photocatalytic reaction kinetics and overall energy conversion efficiency [10, 11]. To address these challenges, various modification strategies, such as elemental doping, defect engineering, and others, have been extensively explored. For instance, by tailoring the electronic structure through band engineering, doping not only extends the material's light absorption into the visible and even near-infrared regions but also enhances charge separation and suppresses carrier recombination [12-14]. Hence, strategies such as elemental doping, heterojunction construction, and defect engineering are commonly employed to tailor the physicochemical properties of g-C_3N_4, thereby enabling efficient and selective CO_2 conversion, a promising avenue for future applications.

The LSPR effect has emerged as a powerful strategy to enhance photocatalytic efficiency by promoting light absorption, facilitating charge carrier separation, accelerating surface reaction kinetics, and even modulating product selectivity. When noble metal NPs are coupled with a semiconductor substrate, their LSPR generates strongly enhanced local electromagnetic fields around the nanoparticle surface and adjacent active sites [15]. This phenomenon arises from the collective oscillation of free electrons in resonance with incident photons, enabling the composite system to exhibit intense, broad-spectrum absorption across the visible to near-infrared range. Such optical properties overcome the inherent limitation of conventional semiconductors like TiO_2, which are primarily active only under ultraviolet irradiation. Among plasmonic materials, Au NPs stand out due to their superior stability and tunable optical response. In contrast to Ag, which readily reacts with sulfur or oxygen to form Ag_2S or Ag_2O, Au NPs remain chemically stable under ambient conditions and retain their plasmonic activity over extended periods. Moreover, Au NPs exhibit greater resistance to corrosion in both acidic and alkaline environments compared to Ag and Cu, making them well-suited for operation in complex or harsh reaction systems. Notably, Au NPs display a strong LSPR response in the near-infrared region, beyond the visible-light absorption dominated by Ag NPs, further expanding their utility in solar-driven applications [16-18].

These advantages have spurred significant research interest in Au-based plasmonic photocatalysts. For instance, Huang et al. designed Au NPs anchored Zr/Ti bimetallic oxide solid solutions via crystal engineering, integrating multiple active sites to achieve stepwise photocatalytic CO_2 conversion into syngas and ultimately C_2 hydrocarbons under simulated solar irradiation [19]. Similarly, Fang et al. developed a ternary hybrid system, 2-Au NCs/Au NPs@SnO_2, by decorating Au NPs@SnO_2 core-shell structures with atomically precise Au nanoclusters (NCs) [20]. The synergistic interaction between plasmonic Au NPs and photoexcited SnO_2 enhances visible-light harvesting and promotes efficient separation and migration of photogenerated carriers. Furthermore, electron-rich Au NCs, formed through interfacial charge transfer, serve as active sites that significantly boost the selectivity and efficiency of CO_2 reduction to CO.

Based on the above analysis, this work aims to harness the synergistic effects of elemental doping and the LSPR of noble metals to simultaneously modulate the band structure, broaden the spectral response for enhanced light utilization, and promote efficient charge carrier dynamics, thereby enabling the effective and selective photoreduction of CO_2. To this end, we first synthesized BMNS using boron oxide, melamine, and cyanuric acid as precursors, followed by the photodeposition of plasmonic Au NPs to construct the Au/BMNS-2 composite photocatalyst. Infrared thermal imaging revealed that the incorporation of Au NPs induced a pronounced photothermal effect under irradiation. Notably, the steady-state surface temperature of BMNS (125.0℃) was significantly higher than that of pristine g-C_3N_4 (73.1℃), and further increased upon Au NPs loading, demonstrating a

positive correlation between localized heating and photocatalytic CO_2 reduction performance.

Comprehensive characterization confirmed that boron doping effectively modulates the electronic band structure of carbon nitride, while the spherical morphology affords a larger specific surface area, enhancing CO_2 adsorption capacity and facilitating active site exposure. Additionally, the Au/BMNS-2 composite exhibits significantly improved visible-light absorption, attributed to the combined effects of bandgap narrowing and the LSPR of Au NPs. Interestingly, it was found that, contrary to their typical role as active sites for CO_2 reduction, Au NPs in this system function primarily as electron donors under light irradiation. The photogenerated hot electrons are back-injected from the Au NPs into the BMNS, and combined with the localized photothermal effect, this process significantly enhances the photocatalytic reduction of CO_2.

2. Experimental section

2.1 Preparation of samples

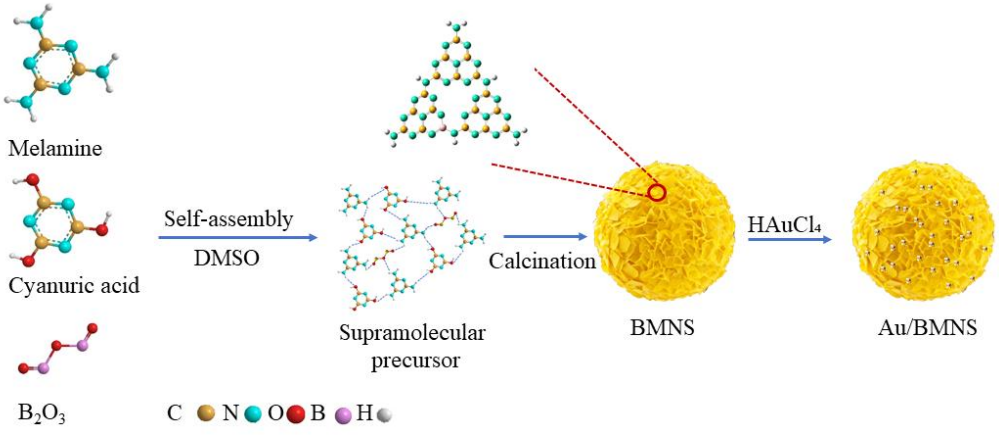

Scheme 1 The synthesis procedure and possible structure of Au/BMNS.

2.2 Synthesis of BMNS

In this study, BMNS was synthesized via a molecular self-assembly strategy using melamine, cyanuric acid, and boron oxide as precursors. The synthetic route is briefly illustrated in Scheme 1. First, melamine, cyanuric acid, and boron oxide are dissolved in a solvent to form a supramolecular precursor. This precursor is then thermally treated at an elevated temperature to yield BMNS. Finally, plasmonic Au NPs are deposited onto the BMNS support via photodeposition, affording the Au/BMNS-x composite photocatalyst. The detailed synthesis procedure is as follows:

First, 0.50 g of cyanuric acid and 0.51 g of melamine were separately dissolved in 20 mL of dimethyl sulfoxide (DMSO). The two solutions were then combined under vigorous stirring, followed by the addition of 1.0 g of boron oxide. The resulting mixture was magnetically stirred for 1.5 h to ensure homogeneity. Afterward, the solution was allowed to stand at room temperature for 12 h to facilitate phase separation and self-assembly of the supramolecular precursor. The precipitate formed during this aging process was collected by vacuum filtration, thoroughly washed three times with anhydrous ethanol to remove residual impurities, and subsequently dried in a vacuum oven at 60℃ for 10 h. The purified precursor was then transferred to a tube furnace and thermally polymerized under a nitrogen atmosphere. The temperature was ramped to 550 ℃ at a controlled rate of 2.3℃ min^{-1} and held isothermally for 4 h. After natural cooling to room temperature within the furnace, the BMNS was obtained as a yellowish solid and ground into a fine powder for further use.

2.3 Synthesis of Au/BMNS Composite:

To prepare the Au NPs-loaded BMNS composite, 0.1 g of BMNS was dispersed in a mixture of 30 mL of deionized water and 2.3 mL of isopropanol in a reaction flask and stirred vigorously for 1 h to ensure uniform dispersion. Subsequently, a precisely measured volume of 10 mg/mL chloroauric acid ($HAuCl_4$) solution was slowly added dropwise under continuous stirring. The reaction mixture was then degassed by purging with nitrogen gas for 30 min to remove dissolved oxygen, followed by irradiation under a

365 nm UV light source for 2 h to facilitate the in situ photoreduction of Au^{3+} ions and the deposition of Au NPs onto the BMNS surface. The resulting product was collected by centrifugation, washed thoroughly with ethanol and deionized water (three times each) to remove unreacted species, and dried overnight at 60 °C under vacuum. The final composite was obtained as a reddish-brown solid and denoted as Au/BMNS-x, where "x" represents the volume of the $HAuCl_4$ solution used during synthesis. The reddish-brown color indicating the LSPR effect of Au NPs.

For comparison, pristine g-C_3N_4 was prepared according to a previously reported method. Briefly, 10 g of melamine was ground uniformly and transferred into a 50 mL crucible, which was then wrapped in aluminum foil to prevent rapid heat loss and minimize sublimation. The crucible was placed in a muffle furnace and heated at a ramping rate of 2.5°C min^{-1} to 550°C, where it was held for 4 h. After cooling naturally to room temperature, the resulting yellow solid was collected and designated as g-C_3N_4.

2.4 General procedure of photocatalytic CO_2 reduction

The photocatalytic CO_2 reduction experiments were carried out in a custom-designed, airtight quartz reactor with a total volume of 300 mL. In a typical procedure, 20 mg of the catalyst was loaded into the reactor. To remove residual air and ensure a pure reaction atmosphere, the system was purged with high-purity CO_2 mixed with water vapor for 20 min, allowing sufficient time for CO_2 adsorption-desorption equilibrium to be established on the catalyst surface. A 300 W xenon lamp, operating at a current intensity of 10 A, was used as the simulated solar light source. During the reaction, gas samples were collected from the headspace of the reactor at hourly intervals over a 4-hour period. The evolved gaseous products were quantitatively analyzed using a gas chromatograph (GC7890, Nanjing Kejie Instrument) equipped with a flame ionization detector and a mechanizer, enabling precise identification and measurement of carbon-based products such as CO and CH_4.

3. Results and discussions

3.1 Structure characterization

As shown in Fig. 1a, the crystal structures of the catalysts were characterized by XRD. To confirm that the prepared samples indeed resulted from the high-temperature polymerization of the supramolecular precursor, XRD patterns of both melamine and the supramolecular precursor were also recorded. As shown in Fig. 1a, the supramolecular precursor exhibits two distinct diffraction peaks at 10.7° and 27.7°, which are markedly different from those of both melamine and g-C_3N_4. This clearly confirms the successful formation of the supramolecular precursor prior to polymerization. For all prepared samples, diffraction peaks at 12.7° and 27.4° are assigned to the (100) and (002) crystal planes of g-C_3N_4, respectively, corresponding to the in-plane structural repeating units and the interlayer stacking of tri-s-triazine frameworks, indicative of a well-ordered conjugated aromatic system [21]. Compared to pristine g-C_3N_4, the (002) diffraction peak of the BMNS sample exhibits significantly reduced intensity after boron doping. This attenuation is attributed to the partial decomposition of cyanuric acid during synthesis, which disrupts the long-range order of the 2D polymeric framework and reduces the periodic stacking of the tri-s-triazine units upon B incorporation. Furthermore, the introduction of Au NPs further influences the crystallinity of the carbon nitride matrix. The presence of Au NPs alters the local electronegativity of the g-C_3N_4 layers, weakening the interlayer hydrogen bonding and leading to structural disorder, as evidenced by the overall broadening and suppression of the (002) peak [22]. In the XRD pattern of Au/BMNS-2, four additional distinct peaks are observed at 38.2°, 44.5°, 64.5°, and 77.4°, which can be indexed to the (111), (200), (220), and (311) crystal planes of face-centered cubic metallic gold, respectively. These peaks show excellent agreement with the standard reference pattern for Au (JCPDS No. 04-0784), confirming the successful deposition and crystalline nature of the plasmonic Au NPs on the BMNS support [23].

The chemical structure of the samples was further investigated by FT-IR spectroscopy. The FT-IR spectra of Au/BMNS-2, BMNS, and pristine g-C_3N_4 exhibit a high degree of consistency, confirming the preservation of the fundamental carbon nitride framework. Characteristic absorption bands, including the out-of-plane bending vibration of the triazine ring at 810 cm^{-1} and the stretching vibrations of C-N heterocycles in the range of 1200-1600 cm^{-1}, are all indicative of the typical structural features of g-C_3N_4. These results suggest that boron doping and the subsequent loading of Au NPs did not significantly disrupt the skeletal structure of the material, maintaining its core chemical integrity.

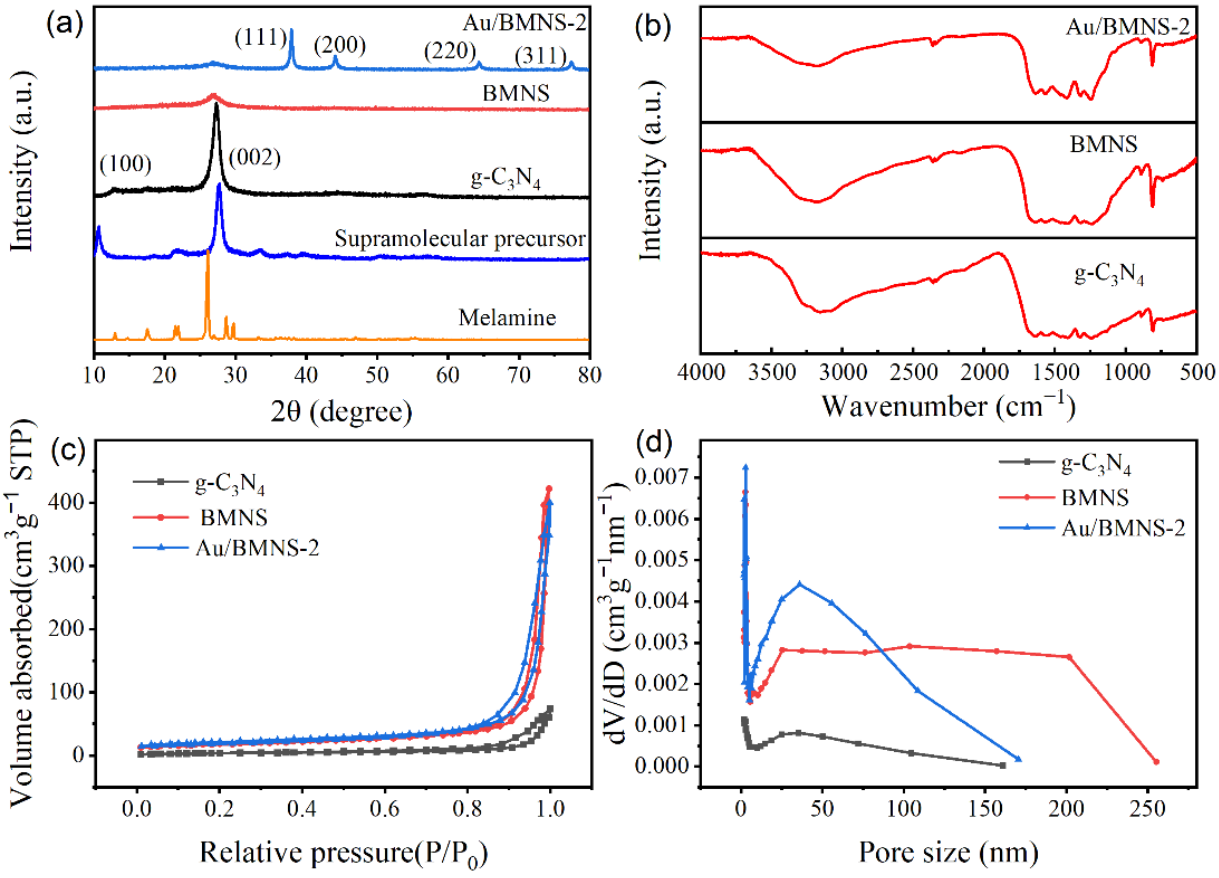

Fig. 1 (a) XRD patterns, (b) FT-IR spectra, (c) N_2 adsorption-desorption isotherms and (d) Pore size distribution of the prepared samples.

Table 1 Structural parameters of the prepared catalysts

Sample	Specific surface area ($m^2 g^{-1}$)	Average pore size (nm)	Pore Volume ($cm^3 g^{-1}$)
g-C_3N_4	13.0799	24.3527	0.1136
BMNS	63.6108	42.3518	0.6530
Au/BMNS-2	72.9416	34.7847	0.6181

The specific surface area and pore structure of the samples were analyzed via N_2 adsorption-desorption isotherms (Fig. 1c). All samples exhibit typical Type IV isotherms with H3-type hysteresis loops, characteristic of mesoporous materials with slit-shaped or plate-like particle aggregates [24]. Notably, BMNS and Au/BMNS-2 display more pronounced hysteresis loops compared to pristine g-C_3N_4, indicating a more developed and interconnected pore channel system. This hierarchical porosity not only enhances light scattering within the material, promoting multiple internal reflections, but also facilitates mass transport of reactants and products during catalysis [25].

Importantly, the unique spherical morphology of BMNS contributes to a significant increase in specific surface area for both BMNS and Au/BMNS-2 (Table 1), thereby exposing a greater number of accessible active sites. The synergistic effect between the enlarged surface area and the well-defined mesoporous architecture enhances light harvesting efficiency by prolonging photon pathlengths and improves the material's capacity for photo-thermal conversion [26]. As a result, the overall photocatalytic activity is substantially boosted.

The morphology of the prepared samples was investigated by SEM and TEM. As shown in Fig. 2a, BMNS, formed via supramolecular self-assembly, exhibits a porous, flower-like spherical architecture composed of interconnected g-C_3N_4 nanosheets. This unique hierarchical structure provides a large specific surface area, which facilitates efficient mass transfer and enhances light harvesting through multiple scattering events. These findings are consistent with the BET surface area analysis and contribute to the improved catalytic performance.

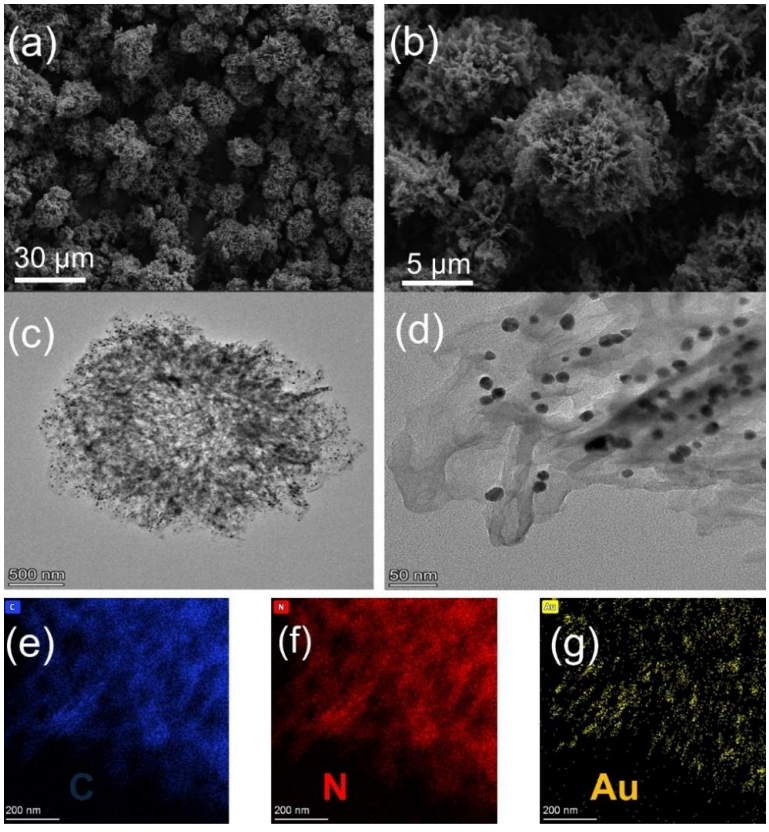

Fig. 2. (a, b) SEM images, (c, d) TEM images, and (e-g) Elemental mapping of Au/BMNS-2.

Figures 2c and 2d reveal that Au NPs are uniformly dispersed on the surface of BMNS, indicating effective anchoring and minimal aggregation. The elemental mapping (Fig. 2e-g) clearly shows the distribution of C, N, and Au elements throughout the composite, confirming the successful incorporation of Au NPs into the BMNS matrix. It should be noted that elemental mapping techniques are generally insensitive to light elements with low atomic numbers. Since B has an atomic number below that of carbon, its presence cannot be reliably detected by conventional EDS mapping. Therefore, the successful doping of B requires further verification through complementary characterization methods.

XPS was employed to systematically investigate the surface elemental composition and chemical states of the prepared samples, as shown in Fig. 3. It is important to note that a positive shift in binding energy (toward higher values) typically indicates a decrease in electron density around the corresponding atom, whereas a negative shift (toward lower values) reflects an increase in electron density. These shifts provide critical insights into electron redistribution and potential charge transfer pathways within the material [27].

The XPS survey spectra (Fig. S1) reveal characteristic signals for C, N, and O in all samples. The C and N signals originate primarily from the g-C_3N_4 framework, while the O signal is likely attributed to surface-adsorbed H_2O or CO_2 molecules. Notably, distinct peaks corresponding to Au are clearly observed in the survey spectrum of Au/BMNS-2, providing direct evidence for the successful loading of Au NPs.

High-resolution C 1s spectra of g-C_3N_4 (Fig. 3a) were deconvoluted into three components: the peak at 288.2 eV is assigned to the N=C-N bond in triazine rings, the peak at 286.2 eV corresponds to the C-NH bonding, and the peak at 284.8 eV arises from adventitious C-C/C=C species [28]. Upon comparison, the binding energies of the C-NH and C-C/C=C components in both BMNS and Au/BMNS-2 remain nearly unchanged relative to pristine g-C_3N_4. However, the N=C-N peak exhibits a clear positive shift, from 288.1 eV in g-C_3N_4 to 288.3 eV in Au/BMNS-2, indicating a reduction in electron density at these carbon sites. This suggests that the carbon atoms within the N-C=N configuration may have been substituted by boron atoms, which are more electron-deficient.

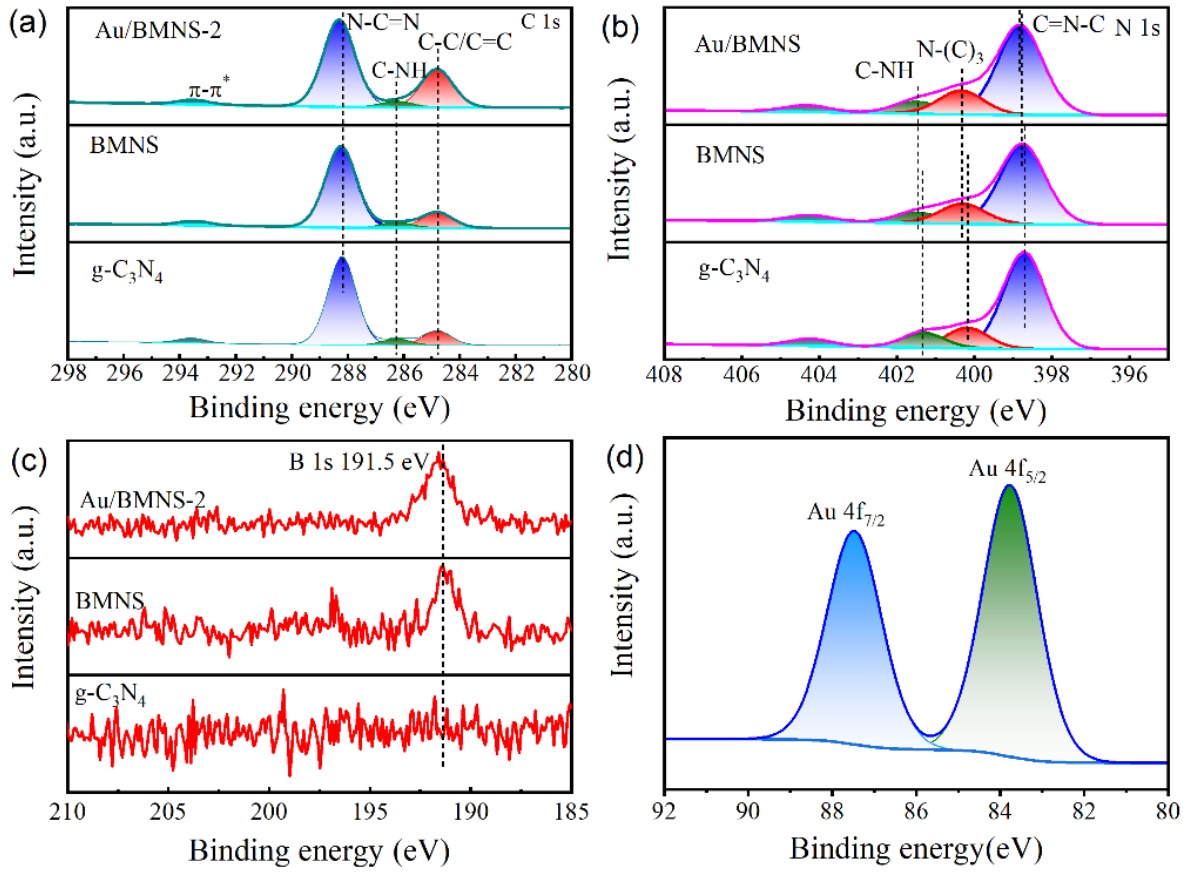

Fig. 3. (a) C 1s, (b) N 1s, (c) B 1s, and (d) Au 4f XPS fine spectra of the prepared catalysts.

The high-resolution N 1s spectrum of g-C_3N_4 (Fig. 3b) can be deconvoluted into three peaks: 398.6 eV (sp^2-hybridized nitrogen in C=N-C, triazine ring), 400.1 eV (tertiary nitrogen, N-(C) $_3$), and 401.3 eV (incompletely condensed amino groups, -NH or -NH_2) [29]. Compared to g-C_3N_4, all three N species in BMNS exhibit a slight but consistent positive shift in binding energy, increasing from 398.7, 400.2, and 401.3 eV to 398.8, 400.3, and 401.5 eV, respectively, indicating a general decrease in electron density on nitrogen atoms. This change is closely associated with boron incorporation, as boron atoms, being electron-deficient, tend to withdraw electron density from neighboring atoms. The uniform shift across all N species suggests that nitrogen atoms may be directly bonded to boron, further supporting the substitution of carbon (in N-C=N) by boron.

Interestingly, in the Au/BMNS-2 sample, only the C=N-C peak shows a noticeable positive shift, while the binding energies of C-NH and N-$(C)_3$ remain largely unchanged. This selective perturbation implies that the Au NPs are preferentially anchored on the triazine ring domains, where they interact electronically with the conjugated π-system. The high-resolution B 1s spectrum (Fig. 3c) shows a distinct peak at 191.5 eV in BMNS and Au/BMNS-2, which is absent in pristine g-C_3N_4. According to Table S1, boron is detected only in the boron doped samples, confirming the successful incorporation of boron into the g-C_3N_4 lattice. Furthermore, the Au 4f spectrum of Au/BMNS-2 (Fig. 3d) displays two well-resolved peaks corresponding to Au $4f_{7/2}$ and Au $4f_{s/2}$. The spin-orbit splitting energy between these doublet peaks is 3.7 eV, which is characteristic of metallic Au^0, confirming the successful reduction and deposition of Au NPs onto the BMNS support [22].

3.2 Optical absorption and band structure

The optical properties of the synthesized samples were investigated using UV-Vis diffuse reflectance spectroscopy (DRS). As shown in Fig. 4a, pristine g-C_3N_4 exhibits relatively weak absorption in the visible light region (500-800 nm), with an absorption edge at

approximately 440 nm, consistent with the intrinsic optical characteristics of conventional g-C_3N_4 semiconductors. In contrast, the BMNS sample displays a pronounced absorption tail extending from 400 to 1000 nm, indicating significantly enhanced light-harvesting capability across a broad range of the visible and near-infrared spectrum. This extended absorption enables more efficient utilization of low-energy photons [30]. Additionally, BMNS shows stronger photo response in the ultraviolet region compared to g-C_3N_4, which can be attributed to its unique morphology. The flocculent porous structure of the BMNS microspheres promotes light scattering and multiple reflections within the material, thereby enhancing photon absorption and facilitating the generation and separation of photogenerated electron-hole pairs [31].

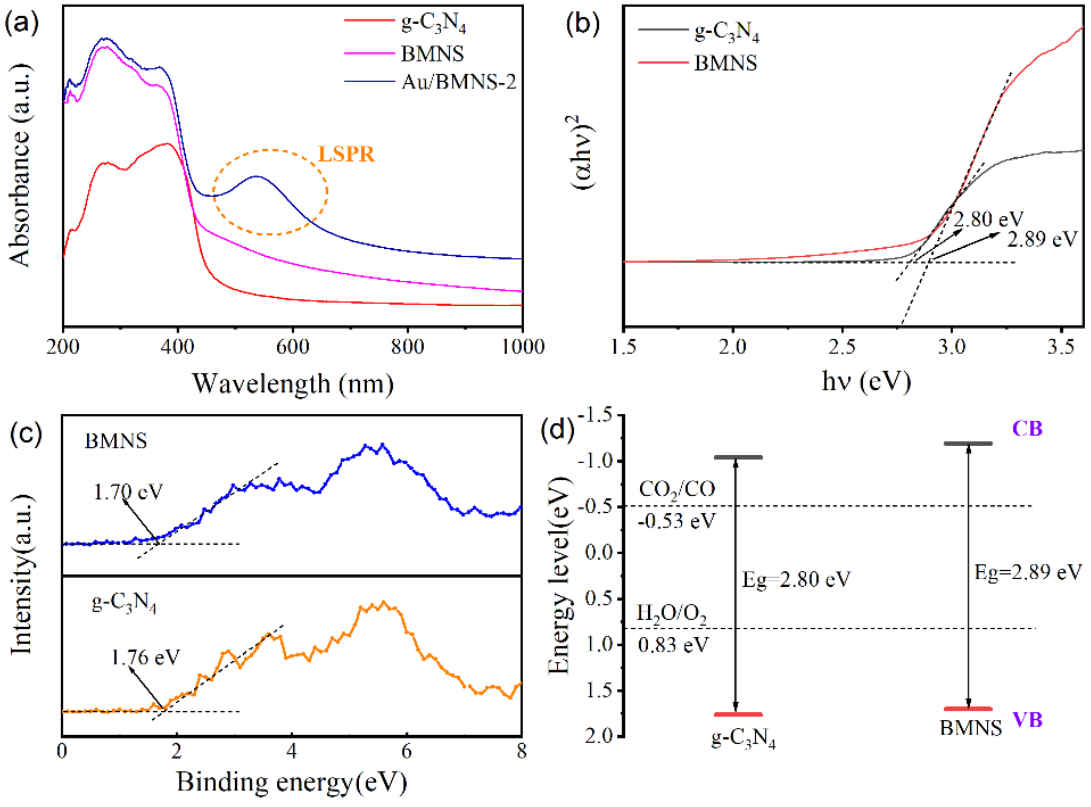

Fig. 4. (a) UV-Vis DRS of the prepared catalysts, (b) Tauc plots, (c) XPS valence band spectra, and (d) band structure of g-C_3N_4 and BMNS.

The band gap energies were estimated from Tauc plots (Fig. 4b), yielding values of 2.80 eV for pristine g-C_3N_4 and 2.89 eV for BMNS. Although the band gap of BMNS is slightly wider, its significantly extended visible-light absorption, evidenced by the broad absorption tail, suggests that mid-gap states or doping-induced sub-band transitions contribute to improved photon harvesting despite the higher E_g.

To determine the precise band energy levels, valence band (VB) positions were measured via XPS valence band spectroscopy. The VB maxima of g-C_3N_4 and BMNS are located at 1.76 eV and 1.70 eV vs. NHE, respectively. Using the relationship $E_{VB} = E_{CB} + E_g$, the conduction band minimum positions were calculated to be −1.04 eV and −1.19 eV vs. NHE for g-C_3N_4 and BMNS, respectively. Notably, the conduction band of BMNS is more negative than that of g-C_3N_4, endowing BMNS with a stronger thermodynamic driving force for reduction reactions, particularly beneficial for CO_2 reduction, which requires highly reducing electrons. Moreover, the VB position of BMNS (1.70 eV) is significantly more positive than the standard potential for water oxidation (0.83 eV vs. NHE at pH 7), providing ample oxidative driving force for water splitting [32]. This favorable band alignment demonstrates that BMNS possesses sufficient thermodynamic potential to simultaneously drive both CO_2 reduction and water oxidation under photoirradiation, making it a promising candidate for overall photocatalytic CO_2 conversion in aqueous environments.

The precise doping of boron not only enables

controllable modulation of the material's band structure but, more importantly, creates efficient interfacial electron transport pathways. This provides an ideal platform for promoting charge separation and transfer during photocatalytic processes [33]. It is well established that boron is an electron-deficient element. When incorporated into the g-C_3N_4 framework, boron atoms introduce DA structural units, which facilitate the spatial separation of photogenerated electrons and holes. This unique electronic configuration promotes the accumulation of electrons and holes at distinct regions of the material, thereby inducing the formation of an internal built-in electric field. This self-driven field significantly enhances charge carrier dynamics by accelerating the separation and migration of photogenerated carriers.

In the case of Au/BMNS-2, a distinct absorption peak is observed near 520 nm (Fig. 4a), which is characteristic of the LSPR effect of Au NPs. Moreover, the plasmonic coupling among Au NPs extends the material's photo response into the near-infrared region (700-1000 nm), greatly enhancing light harvesting across a broad spectral range. This extended absorption not only improves photon utilization but also generates localized heating under irradiation, creating favorable conditions for photo-thermal synergistic catalysis. Moreover, the localized electric field enhancement due to the LSPR effect of Au NPs is also beneficial for the migration of photogenerated charge carriers.

3.3 Photoelectrochemical properties

As a critical kinetic parameter governing the performance of semiconductor photocatalysts, the efficiency of photogenerated charge carrier migration was systematically investigated using photoluminescence (PL) and time-resolved photoluminescence (TRPL) spectroscopy to probe the charge transfer dynamics in the prepared materials. As shown in Fig. 5a, the BMNS composite exhibits a significantly lower PL emission intensity compared to pristine g-C_3N_4 under identical measurement conditions. This pronounced quenching of photoluminescence directly indicates that boron doping effectively suppresses the recombination of photogenerated electron-hole pairs, thereby promoting their spatial separation. This behavior is strong evidence for the formation of DA structural units within the framework [34]. The incorporation of boron alters the hybridization states of atoms in the g-C_3N_4 lattice, inducing a redistribution of electron density and consequently optimizing the material's electronic band structure.

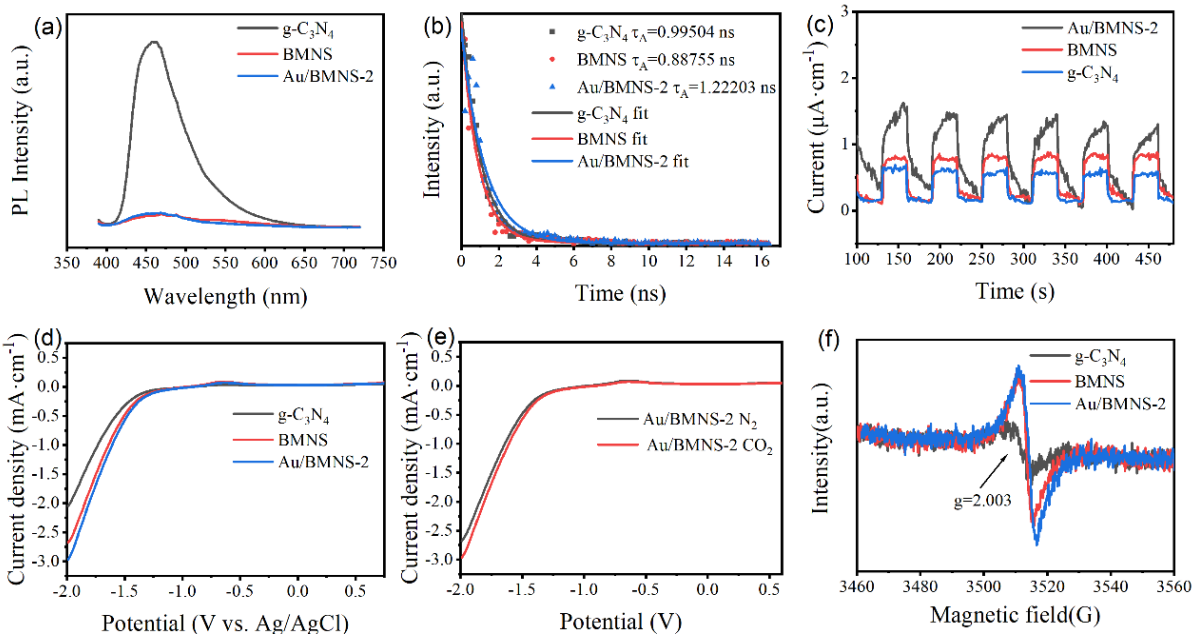

Fig. 5. The obtained PL spectra (a), Time-resolved PL spectra (b), Transient photocurrent response spectroscopy (c), Linear sweep voltammogram (LSV) curves in air (d), LSV curves in N_2 and CO_2 (e), and EPR spectra (f) of the prepared catalysts.

The charge carrier dynamics were further elucidated through TRPL decay analysis (Fig. 5b), with the decay curves fitted using a biexponential function. The results show that the average fluorescence lifetime of BMNS is shorter than that of g-C_3N_4, consistent with the introduction of non-radiative decay pathways

facilitated by boron doping [35]. However, upon Au NPs loading, the average fluorescence lifetime increases, from 0.89 ns in BMNS to 1.22 ns in Au/BMNS-2. This extension of the lifetime indicates that Au NPs provide alternative pathways for electron extraction and storage, effectively prolonging the availability of charge carriers for surface redox reactions, which is particularly beneficial for the kinetically demanding photoreduction of CO_2 [36]. Collectively, the PL and TRPL results demonstrate that the Au/BMNS-2 composite not only exhibits a lower steady-state concentration of photogenerated carriers (due to efficient utilization) but also significantly suppresses radiative and non-productive decay pathways [37]. More importantly, the reduction in non-radiative decay losses enables more effective conversion of absorbed photon energy into thermal energy, thereby enhancing the material's photothermal effect [38]. It is well established that the photothermal effect plays a critical role in boosting the efficiency of CO_2 photoreduction by increasing local temperature, improving reactant adsorption, and accelerating reaction kinetics. This unique energy conversion mechanism provides vital insights into the origin of the enhanced photocatalytic performance in the Au/BMNS-2 system.

The above characterization results demonstrate that Au/BMNS-2 exhibits a lower steady-state concentration of photogenerated electron-hole pairs, indicating highly efficient charge separation. Compared to pristine g-C_3N_4, this composite not only introduces additional non-radiative decay pathways, associated with enhanced charge transfer, but also displays a prolonged fluorescence lifetime. This unique combination of charge dynamics facilitates the effective migration of photogenerated carriers to surface catalytic sites, thereby significantly promoting their participation in the CO_2 photoreduction reaction.

To further evaluate the photoelectrochemical performance and charge transport behavior of the catalysts, transient photocurrent response measurements were conducted. As shown in the Fig. 5c, the photocurrent densities of the three materials follow a clear trend: pristine g-C_3N_4 exhibits the lowest response, BMNS shows a notably enhanced photocurrent, and Au/BMNS-2 delivers the highest photocurrent density among the series. This progressive enhancement strongly corroborates the synergistic effect of boron doping and Au nanoparticle modification in improving the separation and migration efficiency of photogenerated charge carriers [39]. The boron doped structure promotes the formation of efficient electron transport pathways within the framework, while the LSPR effect of Au NPs contributes to the generation of a built-in electric field that further drives the spatial separation of electrons and holes. These electrochemical findings are in excellent agreement with the prior spectroscopic analyses (PL and TRPL), providing consistent and multi-faceted experimental evidence that validates the rationality of the material design strategy [39]. Notably, the superior photoelectrochemical performance of Au/BMNS-2 not only confirms the effectiveness of the boron and Au dual-modification approach but also establishes a solid mechanistic foundation for its high activity in photocatalytic CO_2 reduction. Fig. 5d presents the LSV curves of the prepared samples. Comparative analysis reveals that the onset overpotential of BMNS is significantly lower than that of pristine g-C_3N_4. This reduction is primarily attributed to the enhanced migration and separation of photogenerated charge carriers, which is facilitated by the DA structure engineered through boron doping [40]. Notably, the Au/BMNS-2 sample exhibits the most outstanding electrochemical performance, with a substantially lower overpotential than both BMNS and g-C_3N_4. This improvement is ascribed to the excellent electrical conductivity of Au NPs, which greatly accelerates interfacial charge transport and reduces kinetic barriers [41]. Further LSV measurements under different atmospheres demonstrate that Au/BMNS-2 displays an obvious lower overpotential in CO_2 than in N_2 atmosphere (Fig. 5e), indicating that the CO_2 reduction reaction is kinetically favored on the catalyst surface during the photocatalytic process [42]. The above competitive reaction experiments between CO_2 reduction and proton reduction further confirm that the Au/BMNS-2 system exhibits high selectivity toward CO_2RR, minimizing undesirable side reactions.

EPR spectroscopy reveals a symmetric signal centered at g = 2.003 for all samples (Fig. 5f), characteristic of carbon-centered radicals or delocalized π-electrons. Compared to g-C_3N_4, both BMNS and Au/BMNS-2 exhibit more intense EPR signals, indicating enhanced electron delocalization within the framework. This extended delocalization effectively suppresses charge carrier recombination. Moreover, the strong signal intensity suggests a high concentration of unpaired electrons, which serve as active sites for charge transfer and promote the overall photocatalytic activity [43].

3.4 Photocatalytic CO_2 reduction performance

The photocatalytic CO_2 reduction performance of the synthesized catalysts was systematically evaluated in a

gas-solid phase reaction system. In strict accordance with green chemistry principles, the reaction products were quantitatively analyzed by gas chromatography without the use of any co-catalysts, photosensitizers, or sacrificial reagents. As shown in Fig. 6a and 6b, CO is identified as the sole detectable product, confirming the high selectivity (~100%) of the catalytic process. Under simulated solar irradiation, pristine g-C_3N_4 exhibits a CO evolution rate of 2.38 μmol$g^{-1}h^{-1}$. The boron-doped BMNS catalyst shows significantly enhanced activity, achieving a CO production rate of 5.87 μmol$g^{-1}h^{-1}$, approximately 2.47 times higher than that of the pristine material. Further optimization reveals that the loading amount of Au NPs plays a critical role in determining the performance of the Au/BMNS-x series. Among the samples tested, Au/BMNS-2 delivers the highest photocatalytic activity, with a CO production rate reaching 14.25 μmol$g^{-1}h^{-1}$, which is 5.99 times greater than that of g-C_3N_4. This remarkable enhancement clearly underscores the crucial role of the synergistic effect between boron doping and Au modification in promoting charge separation, improving light utilization, and ultimately boosting the efficiency of photocatalytic CO_2 reduction.

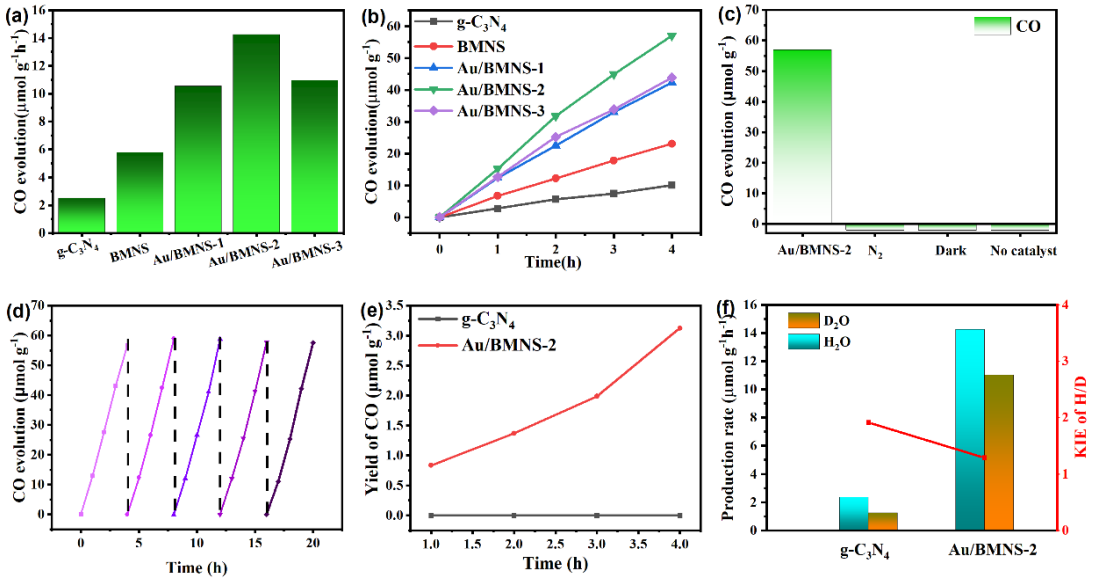

Fig. 6. (a, b) Photocatalytic activity of the prepared catalysts, Reaction conditions: 25°C, 300 W xenon lamp irradiation, 0.02 g of catalyst, CO_2 atmosphere with H_2O vapor. (c) Control experiments for Au/BMNS-2 under varied conditions, (d) Catalytic durability of Au/BMNS-2, (e) The catalytic performance of the catalyst under illumination filtered through a 500 nm cutoff filter, (f) KIE of H/D and production rate over g-C_3N_4, and Au/BMNS-2 in photocatalytic CO_2 reduction.

Systematic control experiments were conducted to investigate the photocatalytic stability and the origin of the CO product over the Au/BMNS-2 catalyst. When the reaction was carried out under a N_2 atmosphere with all other conditions unchanged, no CO was detected, effectively excluding the possibility of CO generation from the decomposition of intrinsic carbon-containing species within the catalyst. Additionally, control experiments carried out under otherwise identical conditions, either in the absence of a catalyst (blank test) or in the dark, both resulted in negligible CO production (Fig. 6c). In addition, a ^{13}C isotope labeling experiment was conducted to unequivocally confirm the carbon source of the observed products (Fig. S3). The detection of ^{13}CO in the final product clearly demonstrates that the generated CO originates from the photoreduction of CO_2, rather than from any carbon-containing contaminants. These results unambiguously demonstrate that CO formation requires the simultaneous presence of three key components: (1) CO_2 as the carbon source, (2) the Au/BMNS-2 catalyst, and (3) light irradiation. To confirm that H_2O rather than any organic component acts as the sacrificial agent, we monitored the evolution of O_2, the oxidation product of H_2O, using a thermal conductivity detector (Fig. S4). A clear O_2 signal was observed, corresponding to a yield of 26.46 μmol·g^{-1} over Au/BMNS-2 within 4 hours. The measured molar ratio of CO to O_2 was 2.15, which closely matches the theoretical value of 2. This agreement strongly confirms that CO_2 reduction proceeds via concomitant oxidation of H_2O. Furthermore, the catalyst exhibited excellent recyclability, maintaining a consistent CO evolution rate over five consecutive photocatalytic

cycles (Fig. 6d). No significant deactivation was observed, indicating high structural and photochemical stability under prolonged reaction conditions. Moreover, the Au/BMNS-2 catalyst after five reaction cycles (Au/BMNS-Re) was characterized by XRD and BET analysis (Fig. S5). The XRD pattern of Au/BMNS-Re closely matches that of the fresh Au/BMNS-2, with only a slight reduction in diffraction peak intensity, indicating excellent structural stability and catalytic durability. Furthermore, BET measurements were carried out to assess any changes in specific surface area before and after the reaction. Notably, the specific surface area of Au/BMNS-Re remains nearly identical to that of the pristine Au/BMNS-2 (Fig. S5b and Table S2), further confirming the robustness of the catalyst's porous structure during the photocatalytic process. These post-reaction characterization results are fully consistent with the observed stability in catalytic activity over multiple cycles. Collectively, these findings confirm that the detected CO originates exclusively from the photocatalytic reduction of CO_2 and highlight the robust stability and reliability of the Au/BMNS-2 catalyst.

In addition, to investigate the influence of light wavelength on catalytic performance, the CO_2 photoreduction reaction was carried out under visible-light irradiation with wavelengths ≥500 nm, using a 500 nm cutoff filter. Under these conditions, no detectable products were formed when g-C_3N_4 was employed as the photocatalyst. In contrast, Au/BMNS-2 yielded 3.12 μmol·g^{-1} of CO under identical conditions (Fig. 6e), underscoring its superior capability to harness lower-energy photons for CO_2 reduction and highlighting the critical dependence of activity on both catalyst design and excitation wavelength.

To further probe the reaction mechanism, a kinetic isotope effect (KIE) study was conducted by replacing H_2O with D_2O while keeping all other reaction parameters unchanged (Fig. 6f). The KIE, defined as the ratio of reaction rates in H_2O versus D_2O (k_H/k_D), serves as a sensitive indicator of whether proton transfer, originating from H_2O dissociation, participates in the rate-determining step during CO_2 photoreduction [44]. Upon isotopic substitution, the reaction rate decreased for both catalysts, as expected when O-H bond cleavage is involved. For g-C_3N_4, a KIE value of 1.91 was obtained, indicating that proton transfer from H_2O dissociation is partially rate-limiting. Strikingly, Au/BMNS-2 exhibited a much smaller KIE of 1.29, suggesting that proton transfer is no longer the slowest step in the catalytic cycle. This marked reduction in KIE implies that the synergistic incorporation of boron and Au NPs significantly accelerates H_2O dissociation and subsequent proton delivery, thereby shifting the rate-determining step away from proton transfer and enhancing overall catalytic efficiency.

Photothermal conversion efficiency is a hallmark characteristic of the LSPR effect. The photothermal conversion capability of the catalysts was evaluated using infrared thermal imaging. As shown in Fig. 7a, all samples exhibit a pronounced photothermal response under standard illumination. During the initial 0-2 min of irradiation, the surface temperature rises rapidly. The heating rate subsequently decreases between 2 and 10 min, and the temperature stabilizes by approximately 15 min. Upon switching off the light, the temperature of each sample quickly returns to its initial value within 5 min, demonstrating excellent reversibility and repeatability of the photothermal effect. A comparison of the temperature-time profiles reveals that Au/BMNS-2 possesses the strongest photothermal conversion efficiency among all samples. It achieves a maximum steady-state temperature of 148.1℃, significantly higher than that of any of the control catalysts. This superior performance highlights the enhanced light-to-heat conversion capability of the Au/BMNS-2 composite, likely due to the synergistic contributions of boron doping and plasmonic Au NPs.

Infrared thermal imaging analysis (Fig. 7b-d) reveals that the steady-state temperature of BMNS is significantly higher than that of pristine g-C_3N_4. This enhancement is primarily attributed to the porous structure formed on the surface of boron-doped spherical carbon nitride, which promotes both light absorption and multiple internal reflections, thereby improving light harvesting efficiency and amplifying the photothermal effect [45]. Notably, upon loading with Au NPs, the steady-state temperature of the catalyst is further elevated, which strongly correlates with its enhanced photocatalytic CO_2 reduction activity [46]. Combined with UV-Vis diffuse reflectance spectroscopy and transient absorption spectroscopy analyses, we propose that this performance improvement arises from synergistic mechanisms: First, the DA architecture induced by boron doping extends the optical response of the catalyst into the near-infrared region (700-1100 nm), significantly enhancing photothermal conversion efficiency. Second, the distinct absorption peak at 520 nm in Fig. 4a confirms the LSPR effect of Au NPs. This LSPR effect not only intensifies the local electromagnetic field but also generates high-energy hot electrons, which can be efficiently injected into the semiconductor matrix. Together, these effects establish a highly efficient photo-thermal-photocatalytic cooperative system that simultaneously boosts charge generation, separation, and energy utilization [47].

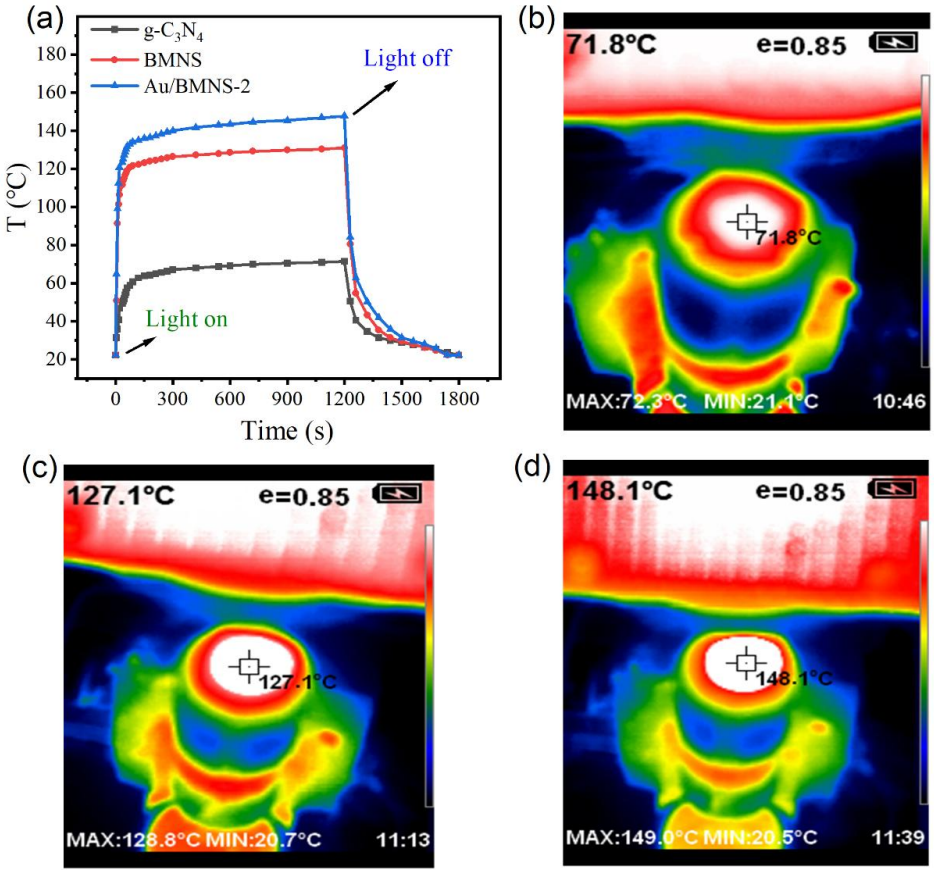

Fig. 7. (a) Temperature response curves of the catalysts corresponding to illumination time (light on → off), (b-d) The stable temperature (20 mg catalyst, gas-solid phase) at 20 min corresponding to the photocatalyst monitored by the thermal imager.

Table 2. Catalytic performance of Au/BMNS-2 compared with other catalysts.

Catalyst	Light source	Sacrificial agent	solvent	Yield (μmol$g^{-1}h^{-1}$)
CN/BOC-OV	UV-vis light	H_2O	–	CO: 4.73/CH_4: 0.77 [48]
PY-CN-5	UV-vis light	H_2O	–	CO: 10.34 [49]
LDH/RGO/CN	UV-vis light	H_2O	–	CO: 10.11/CH_4: 0.5 [50]
NH_2-MIL-101(Fe)/g-C_3N_4	visible-light	TEOA	–	CO: 22.13 [51]
O-CN	UV-vis light	Na_2SO_3	H_2O	CO: 9.44/CH_4: 1.82 [52]
PCN/VN-CTFs	UV-vis light	H_2O	H_2O	CO: 2.83 [53]
This work	UV-vis light	H_2O	–	CO: 14.25

The catalytic performance of Au/BMNS-2 was compared with previously reported g-C_3N_4 based catalysts, as summarized in Table 2. All listed carbon nitride-based catalysts exhibit activity toward photocatalytic CO_2 reduction; however, they differ significantly in product selectivity. For example, CN/BOC-OV and LDH/RGO/CN show only trace CH_4 production, with CO being the dominant product, yet their CO evolution rates are relatively low, 4.73 and 10.11 μmol $g^{-1}h^{-1}$, respectively. When O-CN is used as the catalyst, the CH_4 yield increases to 1.82 μmol $g^{-1}h^{-1}$, but this requires Na_2SO_3 as a sacrificial agent. Other catalysts, such as PY-CN-5 and PCN/VN-CTFs, demonstrate high CO selectivity but suffer from limited CO evolution rates. NH_2-MIL-101(Fe)/g-C_3N_4 achieves a notably high CO evolution rate of 22.13 μmol$g^{-1}h^{-1}$;

however, it relies on triethanolamine (TEOA) as a sacrificial reagent, which compromises its environmental sustainability. In contrast, the Au/BMNS-2 catalyst developed in this work delivers a high CO evolution rate of 14.25 μmol $g^{-1}h^{-1}$ with nearly 100% CO selectivity and utilizes H_2O as the sacrificial agent, rendering the process green and environmentally benign.

3.5 Reaction process and mechanism

The surface reaction mechanism and key intermediates in the photocatalytic CO_2 reduction process over the prepared catalysts were investigated using *in situ* FT-IR. The experiment was conducted under 365 nm irradiation (3 W LED) for 15 min, with CO_2 and H_2O vapor (5 mL/min) introduced into the reaction chamber until equilibrium was established. The spectrum of the pre-irradiation equilibrium system was used as the background, allowing dynamic changes during the reaction to be captured as positive or negative IR signals, which correspond to the formation or consumption of species at the catalyst/H_2O/CO_2 interface, respectively. As shown in Fig. 8a, under dark conditions, the co-adsorption of CO_2 and H_2O at the g-C_3N_4 gas-solid interface gives rise to characteristic IR features. Negative absorption bands in the ranges 3750-3680 cm^{-1} and 3640-3550 cm^{-1} are attributed to the O-H stretching vibrations of physically adsorbed H_2O and surface hydroxyl groups. The intensity of these negative bands increases linearly with time, indicating a progressive decrease in the concentration of surface hydroxyl species. This suggests that the hydroxyl groups undergo chemical transformation upon contact with CO_2 in the dark. The corresponding *in situ* FT-IR spectra of BMNS and Au/BMNS-2 under dark conditions are shown in Fig. S6. All three samples exhibit nearly identical spectral changes in the 3750-3550 cm^{-1} region, indicating that boron doping and Au NPs loading do not significantly alter the initial density or reactivity of surface hydroxyl groups. This preservation of surface hydroxyl chemistry across the catalyst series suggests that the fundamental interface for CO_2 adsorption and activation remains consistent, enabling a reliable comparison of their photocatalytic behaviors.

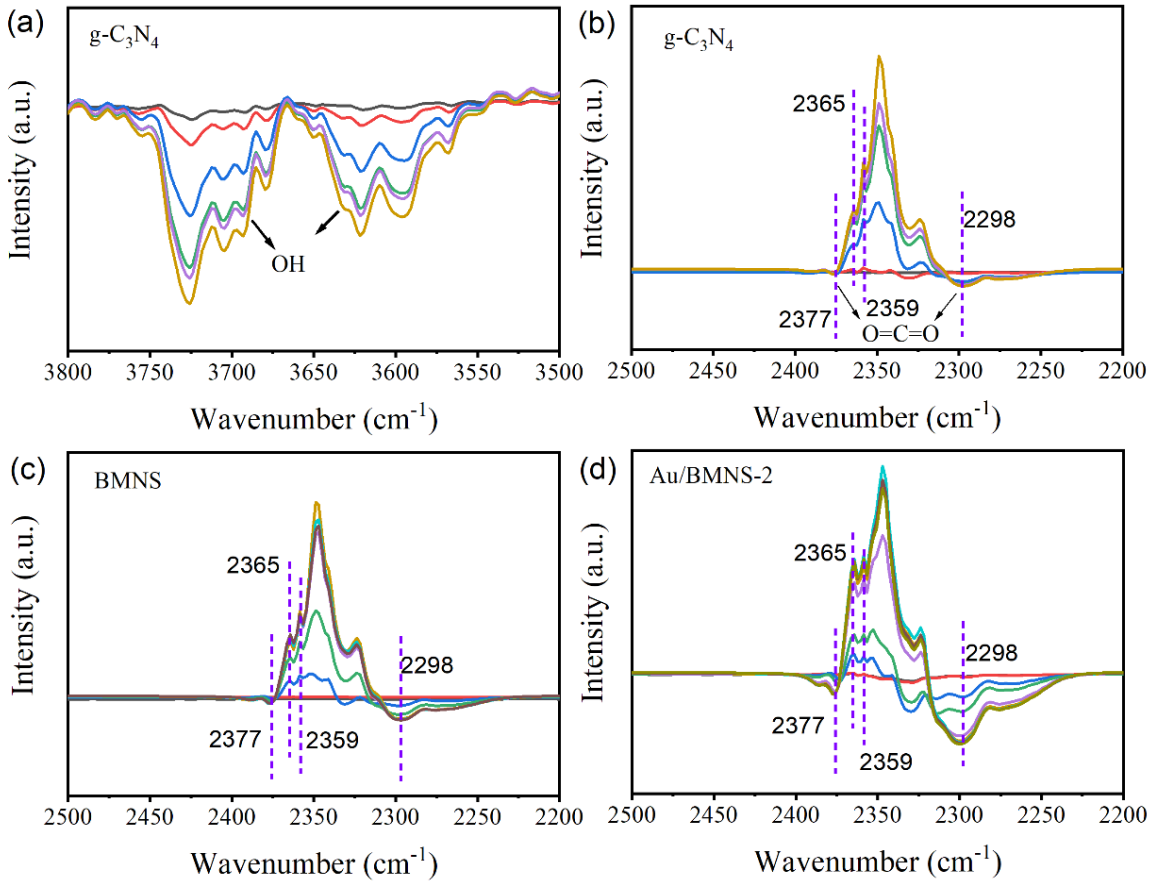

Fig. 8. in situ FT-IR adsorption spectra of the prepared catalysts under dark conditions in a CO_2 + H_2O atmosphere, recorded by DRIFTS. (a) g-C_3N_4 in the wavenumber range of 3500-3800 cm^{-1}; (b) g-C_3N_4, (c) BMNS, and (d) Au/BMNS-2 in the range of 2200-2500 cm^{-1}.

The negative absorption bands at 2298 and 2377 cm^{-1} are attributed to the asymmetric C=O stretching vibrations of physically adsorbed CO_2 on the catalyst surface (Fig. 8b) [54]. These features are barely detectable on pristine g-C_3N_4, indicating weak CO_2 adsorption. However, they become significantly more pronounced upon boron doping, with BMNS exhibiting two distinct negative bands in these regions (Fig. 8c). Upon loading with Au NPs, the band intensities are further enhanced (Fig. 8d), reflecting a substantial increase in CO_2 conversion capacity. These observations suggest that boron doping markedly enhances CO_2 conversion on the catalyst surface, an effect that is further amplified by Au NPs loading. This highlights the synergistic role of both modifications, boron doping and plasmonic metal integration, in promoting the capture and activation of CO_2, which are critical steps preceding its photocatalytic conversion.

Importantly, a positive absorption band emerges at 2365 cm^{-1} in the spectra of BMNS and Au/BMNS-2 (Fig. 8b-d), which can be assigned to a protonated CO_2 intermediate (O=C=O-H^+) [54], most likely the carboxyl species (*COOH) formed via protonation of adsorbed CO_2. This signal intensifies significantly upon incorporation of both boron and Au NPs, indicating enhanced formation of this key intermediate. Upon light irradiation, the positive peak in the 2370-2310 cm^{-1} range gradually diminishes and eventually disappears, while the negative bands associated with physically adsorbed CO_2 (2298 and 2377 cm^{-1}) persist (Fig. S7). This dynamic behavior confirms that the species responsible for the 2365 cm^{-1} band is a reactive intermediate directly involved in the CO_2 reduction pathway, rather than a stable surface species.

Collectively, these *in situ* FT-IR results demonstrate that boron doping and Au NPs loading synergistically enhance both CO_2 adsorption and the formation of the critical intermediate. This dual promotion effect plays a pivotal role in boosting the overall photocatalytic CO_2 reduction performance [55].

Through *in situ* FT-IR analysis (Fig. 9), this study systematically elucidates the photocatalytic CO_2 conversion mechanism on the catalyst surface and identifies key reaction intermediates. Both pristine g-C_3N_4 and Au/BMNS-2 exhibit distinct absorption bands at 1153, 1214, 1301, and 1349 cm^{-1} (Fig. 9a and 9b). The band at 1153 cm^{-1} is assigned to the CH_3O* species, while the peak at 1214 cm^{-1} corresponds to HCO_3^- [10, 56]. The bands at 1301 and 1349 cm^{-1} are attributed to format ($HCOO^-$), a well-established intermediate in CO_2 reduction [35]. These species represent critical intermediates in the CO_2 conversion pathway [56]. Notably, a peak at 1557 cm^{-1} is observed, which confirms the formation of the carboxyl intermediate (COOH), a crucial species in the selective reduction of CO_2 to CO [57]. This supports a reaction pathway in which COOH decomposes into CO, H^+, and an electron (e^-), consistent with the sequence: $CO_2 \rightarrow CO_2^* \rightarrow HCOO^- \rightarrow CO^* \rightarrow CO$ (Eqs. 1-5) [58]. Interestingly, the intensities of the characteristic CO* adsorption bands at 1984 and 2066 cm^{-1} [55, 59] are significantly reduced in Au/BMNS-2 compared to pristine g-C_3N_4, indicating that the CO^* intermediate is rapidly converted rather than accumulated. This suggests that boron doping and Au NPs loading greatly facilitate the desorption of CO^* from the catalyst surface, thereby promoting the formation of the final product.

To gain deeper insight into the spectral changes, expanded FT-IR spectra in the 1100-1500 cm^{-1} region was analyzed for both g-C_3N_4 and Au/BMNS-2 (Fig. 9c and 9d). The peak at 1153 cm^{-1} (CH_3O^*) increases markedly in Au/BMNS-2, indicating enhanced formation of this intermediate upon modification. Furthermore, two new absorption bands appear at 1284 cm^{-1} and 1371 cm^{-1} in Au/BMNS-2, which can be assigned to bidentate (b-CO_3^{2-}) and monodentate (m-CO_3^{2-}) carbonate species, respectively. The emergence of these bands suggests the activation of an alternative reaction pathway involving CO_3 material's intermediates, potentially enabled by the synergistic effect of boron doping and Au NPs incorporation (Eq. 6) [56]. Collectively, the *in situ* FT-IR results demonstrate that the integration of boron and Au NPs not only promotes the protonation of CO_2 and accelerates the conversion of the CO^* intermediate, but also opens up new reaction pathways via CO_3 material's species. These effects synergistically contribute to the significantly enhanced photocatalytic performance of Au/BMNS-2 in CO_2 reduction.

$$Au/BMNS\text{-}2 + h\nu \rightarrow h^+ + e \quad (1)$$

$$HCO_3^- + OH^- \rightarrow CO_3^{2-} + H_2O \quad (2)$$

$$CO_2 + e^- + H^+ \rightarrow HCOO^- \quad (3)$$

$$HCOO^- + e^- + H^+ \rightarrow CO^* + H_2O \quad (4)$$

$$CO^* \rightarrow Co\uparrow \quad (5)$$

$$CO_3^{2-} + 2e^- + 2H^+ \rightarrow 2OH^- + CO\uparrow \quad (6)$$

In situ XPS analysis reveals the distinctive evolution of electronic structure in Au/BMNS-2 under illumination and its critical role in enhancing photocatalytic CO_2 reduction. The results show that, upon light irradiation, the Au 4f peaks shift to higher binding energies by approximately +0.5 eV (Fig. 10c), indicating a decrease in electron density on the gold

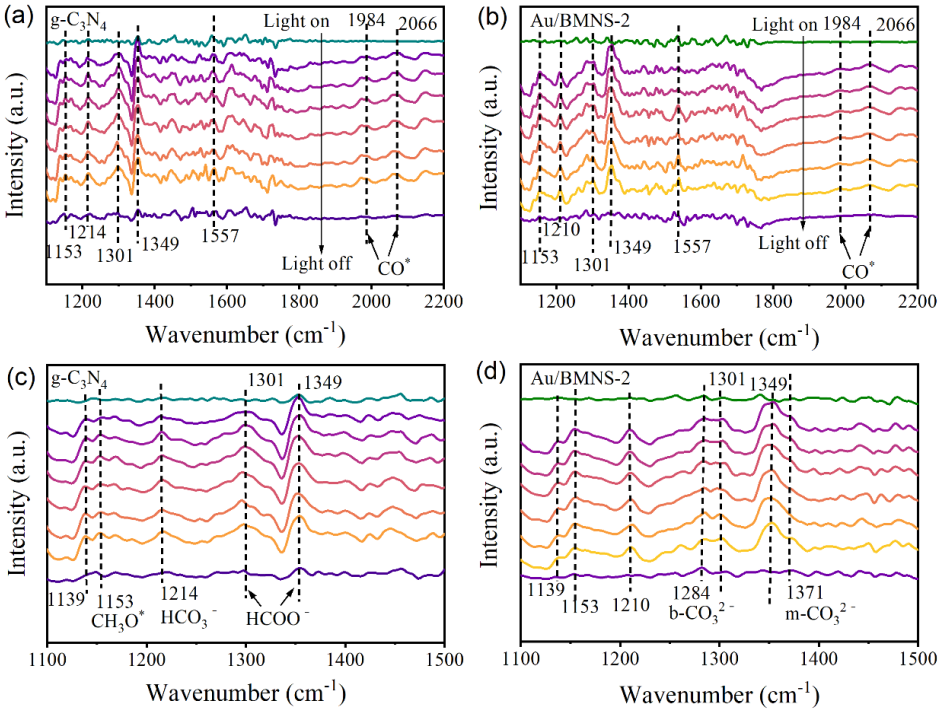

Fig. 9. In situ FT-IR adsorption spectra of the prepared catalysts under light irradiation in a CO_2 + H_2O atmosphere, recorded by DRIFTS. (a) g-C_3N_4, and (b) Au/BMNS-2 in the wavenumber range of 1100-2200 cm^{-1}, (c) g-C_3N_4, and (d) Au/BMNS-2 in the range of 1100-1500 cm^{-1}.

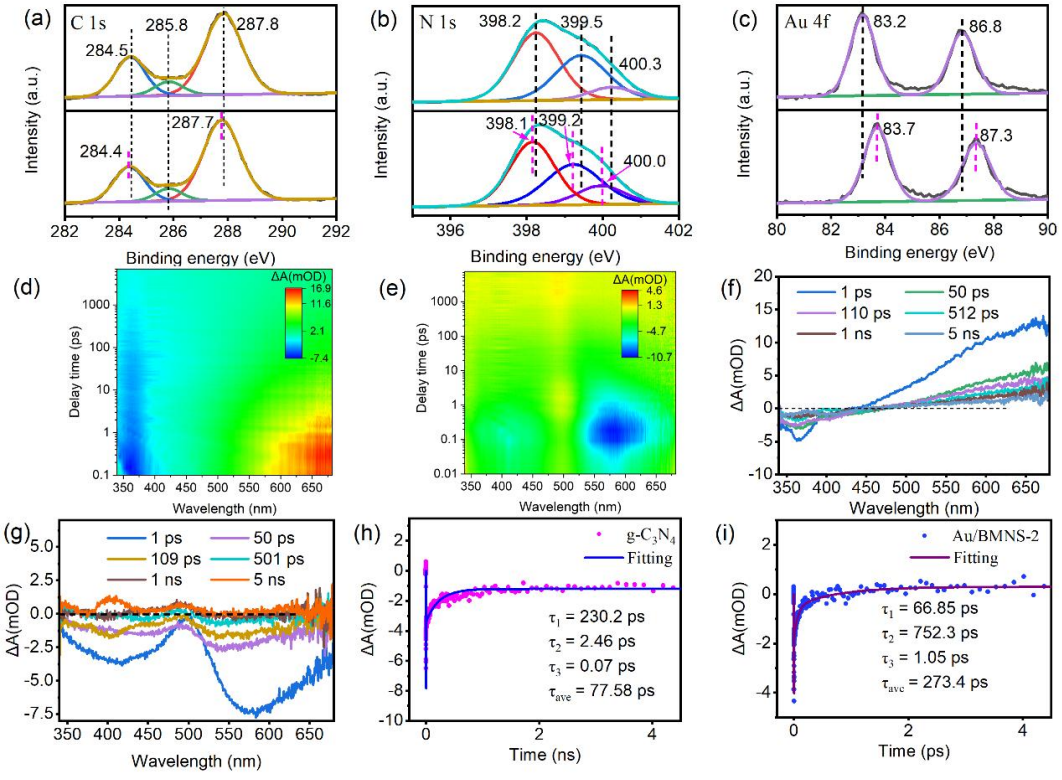

Fig. 10. In situ XPS spectra of (a) C1s, (b) N 1s, and (c) Au 4f. 2D pseudo-color of fs-TA spectra for (d) g-C_3N_4, and (e) Au/BMNS-2. The fs-TAS plots at different delay times for (f) g-C_3N_4, and (g) Au/BMNS-2. Kinetic curves fitted at 365 nm for (h) g-C_3N_4, and (i) Au/BMNS-2.

NPs. Concurrently, the binding energies of C 1s, N 1s, and B 1s in the boron doped g-C_3N_4 framework all shift to lower values (Figs. 10a, 10b, and S8), confirming that the semiconductor gains electrons. Notably, the shifts for carbon and boron species are relatively modest (~0.1 eV), and even the nitrogen atoms within the heptazine rings exhibit only a ~0.1 eV decrease. In stark contrast, the bridging nitrogen atoms between heptazine units, denoted as N(C_3), and the terminal -NH/-NH_2 groups show a pronounced binding energy reduction of up to 0.3 eV, signifying substantial electron accumulation at these specific sites.

This spatially selective electron enrichment clearly demonstrates that, under illumination, electrons are directionally transferred from Au NPs to the g-C_3N_4 matrix, preferentially localizing at nitrogen sites with high electronegativity and lone-pair electrons. These electron-rich N(C_3) and -NH/-NH_2 moieties serve as highly active centers: they not only effectively adsorb and activate inert CO_2 molecules but also supply electrons essential for multi-electron CO_2 reduction pathways. Moreover, boron doping further optimizes the electronic structure of g-C_3N_4, enhancing its capacity to accept and transport injected electrons, thereby synergistically improving interfacial charge transfer efficiency. In summary, the *in situ* XPS data provide direct electronic-structure evidence for a cooperative mechanism in which Au acts as an electron donor, while specific nitrogen sites in g-C_3N_4 function as electron acceptors and catalytic hotspots, offering a fundamental explanation for the superior CO_2 photoreduction performance of Au/BMNS-2.

To determine the direction and dynamics of photogenerated charge carriers, fs-TA spectroscopy was performed on the samples. The 2D pseudo-color maps of g-C_3N_4 and Au/BMNS-2 are shown in Figures 10d and 10e, respectively. Both samples exhibit a distinct signal peak at ~365 nm, assigned to ground-state bleach (GSB), reflecting the depletion of ground-state electrons upon photoexcitation [60, 61]. In pristine g-C_3N_4 (Figures 10d and 10f), a pronounced positive signal ($\Delta OD > 0$) appears in the 450-700 nm region, characteristic of excited-state absorption (ESA) [62]. This ESA signal persists over the entire time window (from 1 ps to 5 ns) and slowly decays, indicating that photogenerated carriers are either trapped in defect states or undergo rapid non-radiative recombination, thereby limiting their availability for surface redox reactions. In contrast, Au/BMNS-2 (Figures 10e and 10g) displays a prominent negative signal ($\Delta OD < 0$) in the 500-650 nm range, which is attributed to stimulated emission (SE) [60]. SE arises from the radiative transition of photoexcited electrons from the first excited singlet state back to the ground state under the influence of the probe pulse. This feature typically appears at wavelengths longer than the ground-state absorption edge of g-C_3N_4 (~450 nm). The presence of SE, instead of ESA, suggests that the incorporation of Au and boron significantly suppresses defect states and non-radiative recombination pathways. Crucially, the SE signal in Au/BMNS-2 gradually decays from 1 ps to 5 ns, reflecting a dynamic depletion of the excited-state population. This decay behavior provides strong evidence that photogenerated electrons are efficiently transferred across the interface and actively consumed in photocatalytic reactions, rather than being lost to recombination.

To probe interfacial electron transfer dynamics at 365 nm, we analyzed the GSB decay kinetics using a triexponential fitting model. This approach yielded three distinct time constants: τ_1, associated with carrier trapping; τ_2, reflecting free carrier or exciton recombination; and τ_3, attributed to radiative or non-radiative recombination involving trap states (Fig. 10h and 10i) [63, 64]. The results reveal that τ_1 for Au/BMNS-2 (66.85 ps) is significantly shorter than that of pristine g-C_3N_4 (230.2 ps), suggesting a markedly accelerated trapping process in the Au and B modified sample. This enhancement likely stems from a reduced exciton binding energy in Au/BMNS-2, which facilitates exciton dissociation and promotes rapid capture of free carriers. In contrast, τ_2 increases dramatically from 2.46 ps in g-C_3N_4 to 752.3 ps in Au/BMNS-2, indicating a substantial suppression of free carrier or exciton recombination. This prolonged lifetime implies more efficient charge separation and greater availability of photogenerated carriers for surface reactions. Furthermore, the τ_3 component in Au/BMNS-2 reaches 1.05 ps, approximately 15 times longer than that of bare g-C_3N_4 (0.07 ps). Given its extended duration, this slow recombination channel is likely linked to long-lived trapped states that can actively participate in subsequent photocatalytic processes, thereby contributing critically to the enhanced CO_2 reduction performance.

Combined with the *in situ* XPS results, it is evident that under illumination, Au NPs undergo LSPR, generating hot electrons that are injected into the CB of BMNS, representing a reverse charge transfer mechanism. In this process, the high-energy injected electrons accumulate in the conduction band of BMNS, while boron doping facilitates spatial charge separation. This effectively suppresses electron-hole recombination, extends the lifetime of photogenerated electrons, and increases the electron density available

for CO_2 reduction. Moreover, the absence of ESA in Au/BMNS-2 further indicates a significant reduction in defect states and a more intact electronic band structure, both of which favor efficient carrier migration toward surface active sites. Additionally, GSB signals observed in the 350-400 nm region are present in both samples, but are notably stronger and more persistent in Au/BMNS-2. This confirms a higher concentration of CB electrons, attributable to dual excitation pathways: (1) intrinsic bandgap excitation of BMNS and (2) plasmon-driven hot electron injection from Au NPs. In summary, the synergistic integration of Au loading and boron doping not only broadens visible-light absorption via the LSPR effect but, more importantly, fundamentally optimizes carrier dynamics through a plasmon-induced reverse electron injection mechanism. This strategy enhances charge separation, prolongs carrier lifetimes, and enables efficient delivery of electrons to adsorbed CO_2 molecules, thereby significantly boosting the photocatalytic CO_2 reduction performance.

DFT simulations were performed to gain deeper insight into the significantly enhanced catalytic performance of Au/BMNS-2. To simplify the computational model, a representative g-C_3N_4 fragment was employed to approximate the extended molecular structure. Analysis of the simulated HOMO and LUMO distributions for pristine g-C_3N_4, BMNS, and Au/BMNS-2 (Fig. 11a) reveals distinct electronic behaviors. In pristine g-C_3N_4, both the HOMO and LUMO are uniformly distributed across the entire molecular framework, indicating that the HOMO and LUMO are localized in the same region. This spatial overlap is unfavorable for the separation of photoinduced electrons and holes, promoting rapid recombination. Upon boron doping, a partial spatial separation of the HOMO and LUMO is observed: the HOMO becomes primarily localized on the heptazine units without boron substitution, while the LUMO is distributed across the fragment, excluding the boron site. This suggests that boron doping induces a degree of charge separation, improving electron-hole separation efficiency. Remarkably, upon loading with Au NPs, a pronounced redistribution of the HOMO and LUMO occurs. The HOMO becomes predominantly localized on the Au NPs and the boron-doped heptazine regions, whereas the LUMO is largely confined to the undoped heptazine units. This clear spatial separation of electron and hole orbitals demonstrates that the synergistic integration of boron and Au NPs effectively promotes the spatial segregation of photogenerated charge carriers. As a result, the recombination of electrons and holes is significantly suppressed, and the migration of photoinduced electrons is greatly accelerated, key factors contributing to the enhanced photocatalytic activity of Au/BMNS-2 [65].

Furthermore, the localized electric field enhancement and the LSPR effect of Au/BMNS-2 under 550 nm excitation were simulated using the finite-difference time-domain (FDTD) method. To facilitate the computation, simplified cross-sectional models of BMNS and Au/BMNS-2 were employed to simulate the distribution of electric field strength. As shown in Fig. 11b, pristine g-C_3N_4 exhibits only weak electric field intensity at the interface when irradiated at 550 nm. In contrast, the Au/BMNS-2 system displays significantly enhanced local electromagnetic field density in the vicinity of the Au NPs. Notably, pronounced plasmonic hot spots emerge in the nanoscale gaps between the Au NPs and the BMNS nanosheet [66], indicating strong confinement of the electromagnetic field and the accumulation of a large number of photoinduced electrons at the interface. These simulation results suggest that, upon excitation, the LSPR of Au NPs efficiently promotes the generation and transfer of hot electrons across the interface. This process effectively suppresses the rapid recombination or relaxation of hot electrons, thereby prolonging their lifetime and enhancing their availability for surface redox reactions. Consequently, the plasmonic effect significantly contributes to the improved photocatalytic performance of Au/BMNS-2 [67, 68]. The FDTD simulations are in excellent agreement with the experimental observations and theoretical analyses, further supporting the critical role of plasmonic enhancement in the catalytic mechanism.

To elucidate the impact of boron doping and Au loading on the electric structure of the prepared catalysts, density of states (DOS) calculations was performed based on idealized structural models of the three catalysts (Fig. S9). As shown in Fig. 11c, g-C_3N_4 and BMNS exhibit similar band structures: the conduction band is primarily composed of N 2p states, while the valence band arises mainly from hybridized N 2p and C 2p orbitals. This aligns with in situ XPS observations, confirming nitrogen sites as key active centers for CO_2 reduction. Upon Au deposition, the Au 5d orbitals participate in the hybridization of both VB and CB, and the Fermi level shifts upward into the valence band. This shift signifies the emergence of metallic character in the Au/BMNS system, which enhances electrical conductivity and facilitates rapid charge transfer, thereby significantly boosting photocatalytic CO_2 reduction activity [69].

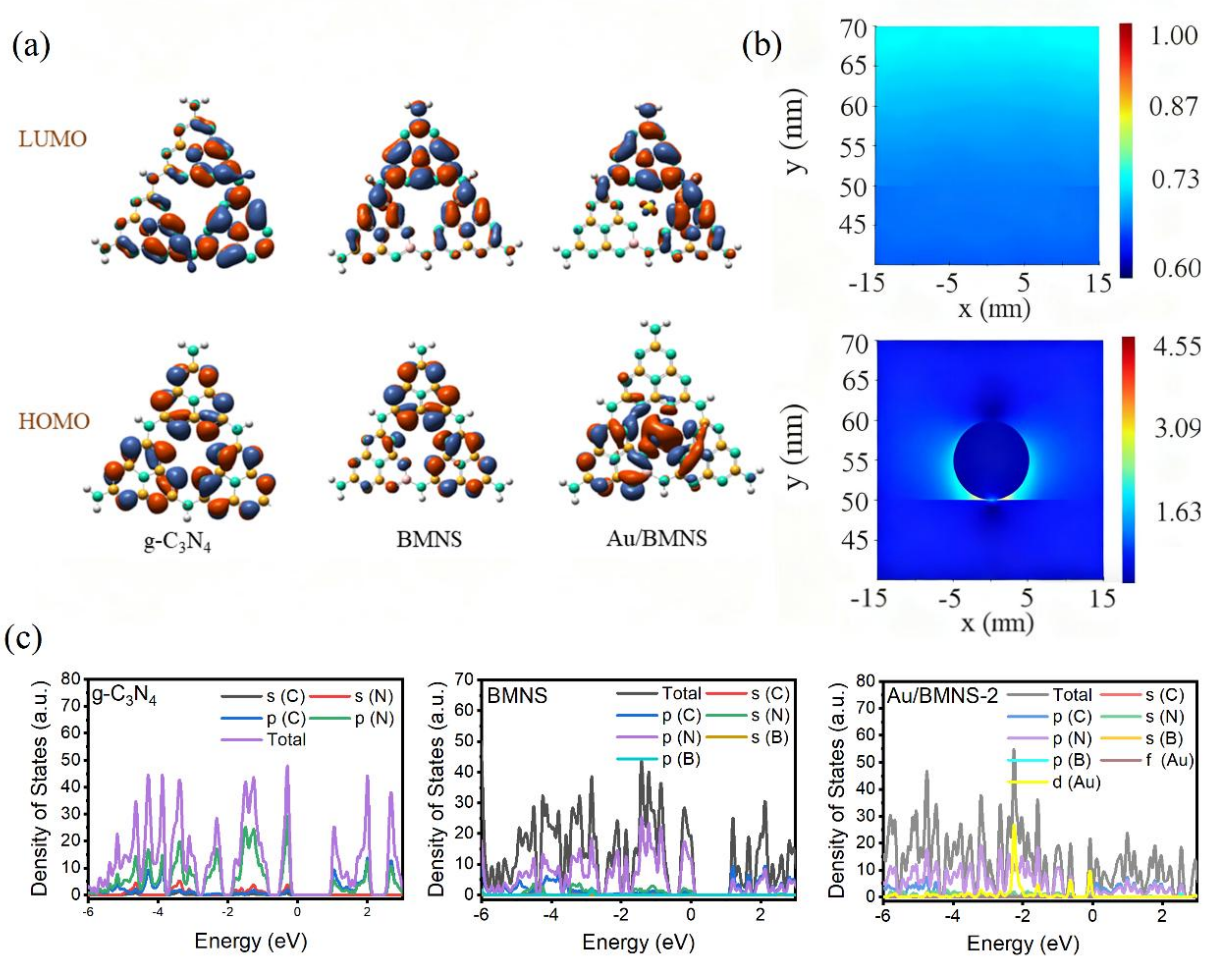

Fig. 11. The simulated HOMO, LUMO distribution (a) of g-C_3N_4, BMNS and Au/BMNS, (b) The FDTD simulated electric field distributions calculated at the cross-sections of BMNS and Au/BMNS with excited light-wavelength at 550 nm, (c) The DOS of the prepared catalysts.

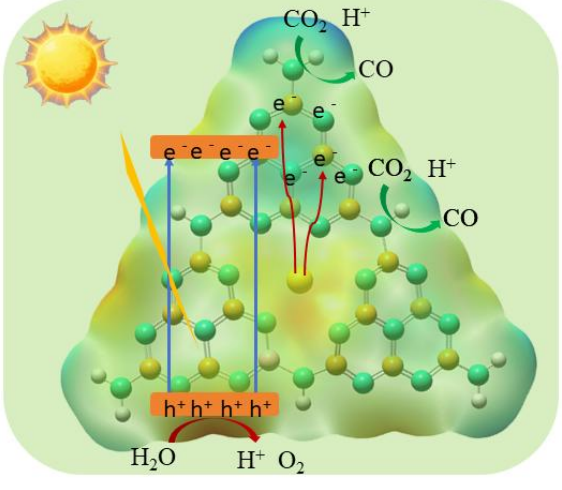

Fig. 12. The possible reaction mechanism of photoreduction CO_2.

Based on the experimental findings and DFT simulation results, a plausible reaction mechanism is proposed and illustrated in Fig. 12. Upon light irradiation, electrons in the HOMO of Au/BMNS-2 are excited to the LUMO. Due to the spatial separation of the HOMO and LUMO, localized on different regions of the catalyst, photogenerated holes accumulate in the HOMO while electrons populate the LUMO, as can be seen from the DFT simulations. Concurrently, the localized electromagnetic field generated by the Au NPs further enhances the accumulation of photoinduced electrons at the interface. Moreover, upon excitation at the plasmon resonance frequency, the Au NPs exhibit strong LSPR, which promotes the generation and interfacial transfer of hot electrons, as indicated by the TDFD and DOS simulations. This process effectively suppresses the rapid recombination

or relaxation of hot carriers, significantly extending their lifetime. As a result, both the photoexcited electrons and the plasmon-generated hot electrons are concentrated on the N sites, which serve as active sites for the synergistic and efficient photoreduction of CO_2. Simultaneously, water molecules are oxidized at the hole-accumulating sites (HOMO region), producing protons and O_2.

4. Conclusion

In this study, g-C_3N_4 was modified through boron doping and morphological engineering to construct a porous spherical structure, designated as BMNS. Subsequently, noble metal Au NPs were deposited onto BMNS via photodeposition to fabricate the composite photocatalyst Au/BMNS-2. Photocatalytic CO_2 reduction experiments demonstrated that Au/BMNS-2 achieves a CO evolution rate of 14.25 $\mu molg^{-1}h^{-1}$, approximately 5.99 times higher than that of pristine g-C_3N_4. The enhanced performance arises from synergistic effects: boron doping and Au NPs loading result in the formation of DA structure, which leads to the spatial separation of HOMO and LUMO, promoting the separation and migration of photoinduced charge carriers. Meanwhile, the Au NPs exhibit strong LSPR absorption across the visible to near-infrared region, enabling efficient hot electron generation and injection at the semiconductor interface. These plasmon-generated hot electrons, together with photoexcited electrons synergistically fulfill the efficient reduction of CO_2.

CRediT author statement

Xianghai Song: Conceptualization, Validation, Writing-original draft, Visualization. Huiling Zhao: Methodology, Investigation, Writing-original draft. Sheng Xu: Methodology, Validation, Writing-original draft. Xiang Liu: Conceptualization, Validation. Mei Wang: Conceptualization, Formal analysis. Weiqiang Zhou: Validation. Jisheng Zhang: Investigation. Yuanfeng Wu: Methodology, Investigation. Panpan Zhang: Validation. Pengwei Huo: Conceptualization, Writing-review & editing, Supervision.

Declaration of competing interest

The authors declare that they have no known competing financial interests or personal relationships that could have appeared to influence the work reported in this article. Pengwei Huo is an Associate Editor of this journal and he was not involved in the editorial review or the decision to publish this article.

Acknowledgments

This work was financially supported by the National Natural Science Foundation of China (Grant no. 22108102)

References

[1] Li X., Wang F., Dong Y., Ho S., Wang C. Quasi-MOFs in water treatment: Synthesis, characterization, and applications, Environmental Science and Ecotechnology, 2026, 29, 100650. https://doi.org/10.1016/j.ese.2025.100650.

[2] Mei R., Wang P., Yi X., Wang C. Engineering MOF-based homojunction photocatalysts for sustainable energy and environment, Environmental Science: Nano, 2025, 12, 5102-5115. https://doi.org/10.1039/D5EN00657K.

[3] Liu Z., Chu H., Yi X., Huang Z., Wang F., Gao Y., Liu X., Li K., Wang C. Photocatalytic reduction of hexavalent chromium by 2D Fe-MOF: mechanistic insights, continuous-flow applications, and ecological safety validation, Environmental Science: Nano, 2025, 12, 5171-5176. https://doi.org/10.1039/D5EN00739A.

[4] Huang N., Li B., Wu D., Chen Z.Y., Shao B., Chen D., Zheng Y.T., Wang W., Yang C., Gu M., Li L., Xu Q. Crystal engineering of MOF-derived bimetallic oxide solid solution anchored with au nanoparticles for photocatalytic CO_2 reduction to syngas and C_2 hydrocarbons. Angewandte Chemie International Edition, 2024, 63(21), e202319177. https:// doi.org/10.1002/anie.202319177.

[5] Shen W., Qi Q., Hu B., Zhu Z., Huo P., Jiang J., Tang X. Studying bimetals copper-indium for enhancing PCN photocatalytic CO_2 reduction activity and selectivity mechanism, Journal of Industrial and Engineering Chemistry, 2025, 145, 384-394. https://doi.org/10.1016/j.jiec.2024.10.033.

[6] Li J., Chai Q., Niu R., Pan W., Chen Z., Wang L., Wang K., Liu Z., Liu Y., Xiao Y., Liu B. Identification of intrinsic vacancies and polarization effect on ternary halo-sulfur-bismuth compounds for efficient CO_2 photoreduction under near-infrared light irradiation, Carbon Energy, 2024, 6, e598. https://doi.org/10.1002/cey2.598.

[7] Jin C., Han B., Luo C., Qin J., Liu Y., Dai Z., Sun Y., Gan Z., Wang C., Zheng X., Hu Z. Precise synthesis of Fe single-atom catalysts on montmorillonite/g-C_3N_4 heterostructures for highly efficient fenton-like degradation of organic pollutants, Water Research, 2025, 287, 124420. https://doi.org/10.1016/j.watres.2025.124420.

[8] Zhang L., Ran J., Qiao S., Jaroniec M. Characterization of semiconductor photocatalysts. Chemical Society Reviews, 2019, 48, 5184-5206. https://doi.org/10.1039/c9cs00172g.

[9] Sadanandan A.M., Yang J.-H., Devtade V., Singh G., Dharmarajan N. Panangattu, Fawaz M., Lee J. Mee, Tavakkoli E., Jeon C.-H., Kumar P., Vinu A. Carbon nitride based nanoarchitectonics for nature-inspired photocatalytic

CO_2 reduction. Progress in Materials Science, 2024, 142, 101242. https://doi.org/10.1016/j.pmatsci.2024.101242.

[10] Gong Y., Chen J., Ma D., Zhong J. Green preparation of nitrogen vacancies enriched g-C_3N_4 for efficient photocatalytic reduction of CO_2 and Cr(VI). Journal of Colloid and Interface Science, 2025, 682, 446-459. https://doi.org/10.1016/j.jcis.2024.11.237

[11] Zhang K., Dan M., Yang J., Wu F., Wang L., Tang H., Liu Z.Q. Surface energy mediated sulfur vacancy of $ZnIn_2S_4$ atomic layers for photocatalytic H_2O_2 production. Advanced Functional Materials, 2023, 33(35), 2302964. https://doi.org/10.1002/adfm.202302964.

[12] Humayun M., Ullah H., Tahir A.A., Yusoff A.R. bin Mohd, Teridi M.A. Mat, Nazeeruddin M.K., Luo W. An overview of the recent progress in polymeric carbon nitride based photocatalysis. The Chemical Record, 2021, 21(7), 1811-1844. https://doi.org/10.1002/tcr.202100067.

[13] Mateo D., Cerrillo J.L., Durini S., Gascon J. Fundamentals and applications of photo-thermal catalysis. Chemical Society Reviews, 2021, 50(3), 2173-2210. https://doi.org/10.1039/d0cs00357c.

[14] Zhang K., Tian L., Yang J., Wu F., Wang L., Tang H., Liu Z.Q. Pauling-type adsorption of O_2 induced by heteroatom doped $ZnIn_2S_4$ for boosted solar-driven H_2O_2 production. Angewandte Chemie International Edition, 2024, 63(5), e202317816. https://doi.org/10.1002/anie.202317816.

[15] Gao B., Dou M., Wang J., Zhuang T., Li P., Yang F., Wang D., Ci L., Fu Y. Effect of carbon nitride synthesized by different modification strategies on the performance of carbon nitride/PVDF photocatalytic composite membranes. Journal of Hazardous Materials, 2022, 422, 126877. https://doi.org/10.1016/j.jhazmat.2021.126877.

[16] Bao X., Lu D., Wang Z., Yin H., Zhu B., Chen B., Shi M., Zhang Y., Xu Q., Qin Y., Shen X.-C., Wu K. Significantly enhanced photothermal catalytic CO_2 reduction over TiO_2/g-C_3N_4composite with full spectrum solar light. Journal of Colloid and Interface Science, 2023, 638, 63-75. https://doi.org/10.1016/j.jcis.2023.01.096.

[17] Shi R., Cao Y., Bao Y., Zhao Y., Waterhouse G.I.N., Fang Z., Wu L.Z., Tung C.H., Yin Y., Zhang T. Self-assembled Au/CdSe nanocrystal clusters for plasmon-mediated photocatalytic hydrogen evolution, Advanced Materials, 29 (2017) 1700803. https://doi.org/10.1002/adma.201700803.

[18] Zhou C., Shang L., Yu H., Bian T., Wu L. Z., Tung C. H., Zhang T. Mesoporous plasmonic Au-loaded Ta_2O_5 nanocomposites for efficient visible light photocatalysis, Catalysis Today, 2014, 225, 158-163. https://doi.org/10.1016/j.cattod.2013.10.085.

[19] Soltan W. Ben, Abdalla M., Harrath K., Peng J., Zhang Y., Cao Z., Liu H. Preparation of LSPR enhanced Z-scheme Pd/WO_3@SnO_2 for photocatalytic decomposition of organic compounds under simulated sunlight. Journal of Environmental Chemical Engineering, 2023, 11(5), 110637. https://doi.org/10.1016/j.jece.2023.110637.

[20] Boruah P.J., Kalita P., Bailung H. Synergistic role of oxygen vacancy defect and plasmonic on modulating the photocatalytic activity of Ag/CuO_x nanocomposites synthesized via solution plasma. Surfaces and Interfaces, 2023, 43, 103539. https://doi.org/10.1016/j.surfin.2023.103539.

[21] Cao G., Xing H., Gui H., Yao C., Chen Y., Chen Y., Li X. Plasmonic quantum dots modulated nano-mineral toward photothermal reduction of CO_2 coupled with biomass conversion. Nano Research, 2024, 17(6), 5061-5072. https://doi.org/10.1007/s12274-024-6521-9.

[22] Che Y., Weng B., Li K., He Z., Chen S., Meng S. Chemically bonded nonmetallic LSPR S-scheme hollow heterostructure for boosting photocatalytic performance. Applied Catalysis B: Environment and Energy, 2025, 361, 124656. https://doi.org/10.1016/j.apcatb.2024.124656.

[23] Chen C., Wu M., Xu Y., Ma C., Song M., Jiang G. Efficient photoreduction of CO_2 to CO with 100% selectivity by slowing down electron transport. Journal of the American Chemical Society, 2024, 146(13), 9163-9171. https://doi.org/10.1021/jacs.3c14590.

[24] Chen J., Ren Y., Fu Y., Si Y., Huang J., Zhou J., Liu M., Duan L., Li N. Integration of Co single atoms and Ni clusters on defect-rich ZrO_2 for strong photothermal coupling boosts photocatalytic CO_2 reduction. ACS Nano, 2024, 18(20), 13035-13048. https://doi.org/10.1021/acsnano.4c01637.

[25] Li Z., Zi J., Luan X., Zhong Y., Qu M., Wang Y., Lian Z. Localized surface plasmon resonance promotes metal-organic framework-based photocatalytic hydrogen evolution. Advanced Functional Materials, 2023, 33(33), 2303069. https://doi.org/10.1002/adfm.202303069.

[26] Dharmarajan N.P., Vidyasagar D., Yang J.H., Talapaneni S.N., Lee J., Ramadass K., Singh G., Fawaz M., Kumar P., Vinu A. Bio-inspired supramolecular self-assembled carbon nitride nanostructures for photocatalytic water splitting. Advanced Materials, 2024, 36(2), 2306895. https://doi.org/10.1002/adma.202306895.

[27] Sheng J., He Y., Li J., Yuan C., Huang H., Wang S., Sun Y., Wang Z., Dong F. Identification of halogen-associated active sites on bismuth-based perovskite quantum dots for efficient and selective CO_2-to-CO photoreduction. ACS Nano, 2020, 14(10), 13103-13114. https://doi.org/10.1021/acsnano.0c04659.

[28] Ji S., Qu Y., Wang T., Chen Y., Wang G., Li X., Dong J., Chen Q., Zhang W., Zhang Z., Liang S., Yu R., Wang Y., Wang D., Li Y. Rare-earth single erbium atoms for enhanced photocatalytic CO_2 reduction. Angewandte Chemie International Edition, 2020, 59(26), 10651-10657. https://doi.org/10.1002/anie.202003623.

[29] Shi X., Huang Y., Bo Y., Duan D., Wang Z., Cao J., Zhu G., Ho W., Wang L., Huang T., Xiong Y. Highly selective photocatalytic CO_2 methanation with water vapor on single-atom platinum-decorated defective carbon nitride.

Angewandte Chemie, 2022, 134(27), 202203063. https://doi.org/10.1002/ange.202203063.

[30] Xia Y., Yang H., Ho W., Zhu B., Yu J. Promoting the photocatalytic NO oxidation activity of hierarchical porous g-C_3N_4 by introduction of nitrogen vacancies and charge channels. Applied Catalysis B: Environmental, 2024, 344, 123604. https://doi.org/10.1016/j.apcatb.2023.123604.

[31] Liu Z., Li Y., Yao S., Zhou R., Lin G., Fu Y., Zhou Q., Wang W., Chi W. Rich electron delocalization structure in carbon nitride inducing radical transfer for high-performance photocatalytic uranyl reduction. Carbon Energy, 2024, 6(12), 636. https://doi.org/10.1002/cey2.636.

[32] Hong L., Guo R., Yuan Y., Ji X., Lin Z., Gu J., Pan W. Urchinlike $W_{18}O_{49}$/g-C_3N_4 Z-scheme heterojunction for highly efficient photocatalytic reduction of CO_2 under full spectrum light. Energy & Fuels, 2021, 35(14), 11468-11478. https://doi.org/10.1021/acs.energyfuels.1c01241.

[33] Zhou Z., Tang R., Li L., Xiong S., Zeng H., Zheng J., Gong D., Huang Y., Deng Y. $W_{18}O_{49}$-based photocatalyst: Enhanced strategies for photocatalysis employment. Separation and Purification Technology, 2023, 319, 124028. https://doi.org/10.1016/j.seppur.2023.124028.

[34] Ma Z., Zhang L., Ma X., Shi F. Z-scheme g-C_3N_4/Bi/$Bi_{3.64}Mo_{0.36}O_{6.55}$ photocatalyst with dual charge transfer channels: Photodegradation of pollutants and mechanism insights. Separation and Purification Technology, 2022, 297, 121435. https://doi.org/10.1016/j.seppur.2022.121435.

[35] Li G., Wu Y., Wang M., Zhou W., Liu X., Zhu Z., Song X., Huo P. Graphitic carbon nitride modified with 2-aminothiophene-3-carbonitrile to boost molecular dipole and $n \rightarrow \pi^*$ electronic transition for photoreduction of carbon dioxide. ACS Applied Nano Materials, 2023, 6(15), 14513-14526. https://doi.org/10.1021/acsanm.3c02600.

[36] Chang X., Wang T., Gong J. CO_2 photo-reduction: Insights into CO_2 activation and reaction on surfaces of photocatalysts. Energy & Environmental Science, 2016, 9(7), 2177-2196. https://doi.org/10.1039/c6ee00383d.

[37] You F., Zhou Y., Li D., Zhang H., Gao D., Ma X., Hao R., Liu J. Construction of a flower-like SnS_2/SnO_2 junction for efficient photocatalytic CO_2 reduction. Journal of Colloid and Interface Science, 2023, 629, 871-877. https://doi.org/10.1016/j.jcis.2022.09.134.

[38] Cui H., Cao J., Zhao Y., Wang J., Li S., Ge K., Chen J., Yang Y. Construction of IO-B-TiO_2/In_2O_3 S-scheme heterojunction with photothermal effects and its highly efficient photocatalytic reduction of CO_2 under full-spectrum light. Chemical Engineering Journal, 2024, 479, 147618. https://doi.org/10.1016/j.cej.2023.147618.

[39] Hong J., Jeon Y.E., Park J., Kim Y.E., Ko Y.N. Synergistic effect of hybrid support with carbon nitride and carbon black on ag catalyst for efficient CO_2 reduction to CO. Applied Surface Science, 2025, 696: 162892. https://doi.org/10.1016/j.apsusc.2025.162892.

[40] Saini P., Kumar K., Saini S., Sethi M., Meena P., Gurjar A., Parewa W. Weigand, V. Photocatalytic single electron reduction of CO_2 into carbon dioxide radical anion ($CO_2^{\cdot-}$): Generation, detection and chemical utilization. Journal of Energy Chemistry, 2025, 105, 525-559. https://doi.org/10.1016/j.jechem.2025.02.013.

[41] Liu B., Sun S., Song Y., Song H., Lin W. Enhanced photocatalytic CO_2 reduction to CH_4 via phosphorus-doped carbon nitride with Cu-Cu coordinated sites. Applied Surface Science, 2025, 687, 162153. https://doi.org/10.1016/j.apsusc.2024.162153.

[42] Gan Y., Osgouei A. Kalantari, Ahrens A., Wang B., Zhou J., Zhan J.-Z., Zeng D., Nie S., Zhao X., Chen G., Nordlander P., Zhou L. 2D plasmonic photocatalyst enables highly efficient hot-electron-mediated surface reactions under red light irradiation. ACS Nano, 2025, 19(17), 17006-17013. https://doi.org/10.1021/acsnano.5c03598.

[43] Ding C., Yang L., Lu X., Chi H., Yang Y., Zhang Y., Yuan J., Wang X., Zhou Y., Zou Z. Synergistic effect of asymmetric Ru-Pd dual single-atom-sites and Pd nanoparticles on carbon nitride for efficient CO_2 photoreduction. Applied Catalysis B: Environment and Energy, 2025, 365, 124917. https://doi.org/10.1016/j.apcatb.2024.124917.

[44] Liu P., Huang Z., Gao X., Hong X., Zhu J., Wang G., Wu Y., Zeng J., Zheng X. Synergy between Palladium Single Atoms and Nanoparticles via Hydrogen Spillover for Enhancing CO_2 Photoreduction to CH_4, Advanced Materaterials, 2022, 34, e2200057. https://doi.org/10.1002/adma.202200057.

[45] Verma R., Sharma G., Polshettiwar V. The paradox of thermal vs. non-thermal effects in plasmonic photocatalysis. Nature Communications, 2024, 15(1), 7974. https://doi.org/10.1038/s41467-024-51916-3.

[46] Fan Z., Wu Y., Luo Y., Qin Y., Xie Y., Ling Y., Wang Y. Synergistic effect between ohmic contacts and localized surface plasmon resonance for enhancing CO_2 photoreduction of BiOBr. Separation and Purification Technology, 2025, 352, 128230. https://doi.org/10.1016/j.seppur.2024.128230.

[47] Yang Q., Tian Q., Li X., Zhu Y., Fang G. Plasmonic active “hot carriers” facilitating photocatalytic CO_2reduction and 2, 4-dichlorophenol oxidation over Bi-deposited BiOBr with abundant oxygen vacancies. Separation and Purification Technology, 2024, 332, 125775. https://doi.org/10.1016/j.seppur.2023.125775.

[48] Chen Y., Wang F., Cao Y., Zhang F., Zou Y., Huang Z., Ye L., Zhou Y. Interfacial oxygen vacancy engineered two-dimensional g-C_3N_4/BiOCl heterostructures with boosted photocatalytic conversion of CO_2, ACS Applied Energy Materials, 2020, 3, 4610-4618. https://doi.org/10.1021/acsaem.0c00273.

[49] Song X., Mao W., Wu Y., Wang M., Liu X., Zhou W., Huo P. Fabricating carbon nitride-based 3D/0D intramolecular donor-acceptor catalysts for efficient photoreduction of CO_2, New Journal of Chemistry, 2022, 46, 20225-20234.

https://doi.org/10.1039/D2NJ04502H.

[50] Yang Y., Wu J., Xiao T., Tang Z., Shen J., Li H., Zhou Y., Zou Z. Urchin-like hierarchical CoZnAl-LDH/RGO/g-C_3N_4 hybrid as a Z-scheme photocatalyst for efficient and selective CO_2 reduction, Applied Catalysis B: Environmental, 2019, 255, 117771. https://doi.org/10.1016/j.apcatb.2019.117771.

[51] Dao X., Xie X., Guo J., Zhang X., Kang Y., Sun W. Boosting Photocatalytic CO_2 Reduction Efficiency by Heterostructures of NH_2-MIL-101(Fe)/g-C_3N_4, ACS Applied Energy Materials, 2020, 3, 3946-3954. https://doi.org/10.1021/acsaem.0c00352.

[52] Zhu Z., Shen W., Li D., Ye J., Song X., Tang X., Zhao J., Huo P. Oxygen-doped red carbon nitride: enhanced charge separation and light absorption for robust CO_2photoreduction, Inorganic Chemistry, 2023, 62, 15432-15439. https://doi.org/10.1021/acs.inorgchem.3c01633.

[53] Zhang P., Jia J., Wang Y., Tong L., Wang J., Li C., Dong H. Metal-free 2D/2D VdW heterojunction fabricated by amorphous covalent triazine frameworks with nitrogen-defect on polymeric carbon nitride towards enhanced photocatalytic performance, Separation and Purification Technology, 2024, 330, 125224. https://doi.org/10.1016/j.seppur.2023.125224.

[54] Yin S., Zhou Y., Liu Z., Wang H., Zhao X., Zhu Z., Yan Y., Huo P. Elucidating protonation pathways in CO_2 photoreduction using the kinetic isotope effect. Nature Communications, 2024, 15(1), 437. https://doi.org/10.1038/s41467-024-44753-x.

[55] Li J., Li K., Du J., Yang H., Song C., Guo X. Impact of transition metal incorporation on the photocatalytic CO_2 reduction activity of polymeric carbon nitride. Journal of CO_2Utilization, 2022, 64, 102162. https://doi.org/10.1016/j.jcou.2022.102162.

[56] Yang J., Hou Y., Sun J., Liang T., Zhu T., Liang J., Lu X., Yu Z., Zhu H., Wang S. Cu doping and Ti_3C_2OH quantum dots co-modifications of $Zn_3In_2S_6$ boosted photocatalytic reduction of CO_2 to CO via accelerating carriers transfer and enhancing CO_2 adsorption and activation. Chemical Engineering Journal, 2023, 452, 139522. https://doi.org/10.1016/j.cej.2022.139522.

[57] Yang Y., Li F., Chen J., Fan J., Xiang Q. Single Au atoms anchored on amino-group-enriched graphitic carbon nitride for photocatalytic CO_2 reduction. ChemSusChem, 2020, 13(8), 1979-1985. https://doi.org/10.1002/cssc.202000375.

[58] Li S., Yang Y., Wan S., Wang R., Yu M., Song F., Zhong Q. Supramolecular self-assemble deficient carbon nitride nanotubes for efficient photocatalytic CO_2 reduction. Journal of Colloid and Interface Science, 2023, 651, 726-733. https://doi.org/10.1016/j.jcis.2023.08.042.

[59] Zu X., Zhao Y., Li X., Chen R., Shao W., Li L., Qiao P., Yan W., Pan Y., Xu Q., Zhu J., Sun Y., Xie Y. Reversible switching Cu^{II} /Cu^{I} single sites catalyze high-rate and selective CO_2 photoreduction. Angewandte Chemie, 2023, 135(1), e202215247. https://doi.org/10.1002/ange.202215247.

[60] Yang X., Ren L., Jiang D., Yin L., Li Z., Yuan Y. Strong interfacial chemical bonding in regulating electron transfer and stabilizing catalytic sites in a metal-semiconductor schottky junction for enhanced photocatalysis, Small, 2023, 20, 2308408. https://doi.org/10.1002/smll.202308408.

[61] Huang Y., Zhang J., Ruzimuradov O., Mamatkulov S., Dai K., Low J. Selective oxygen vacancy engineering for shrinking the potential barrier of S-scheme heterojunction toward highly efficient photocatalytic CO_2 conversion, Composite Functional Materials, 2025, 1, 20250103. https://doi.org/10.63823/20250103

[62] Li Y., Su W., Yang Y., Bai L., Lu J., Zhang W., Wei S. *In situ* topotactic formation of the pn-type inorganic intergrowth bulk heterojunction NiO(Al)/CuO(Ni, Al) for photocatalytic CO_2 methanation, Applied Catalysis B: Environmental, 2024, 341, 123282. https://doi.org/10.1016/j.apcatb.2023.123282

[63] Ai M., Pan L., Shi C., Huang Z.-F., Zhang X., Mi W., Zou J.-J. Spin selection in atomic-level chiral metal oxide for photocatalysis, Nature Communications, 2023, 14, 4562. https://doi.org/10.1038/s41467-023-40367-x

[64] Shi H., Liu H., Du C., Zhong F., He Y., Guro V.P., Zhou Y., Sheng J., Dong F. Unlocking Spatially Constrained Photogenerated Charge via Dimension Regulation in Metal Halide Perovskite Nanowires for Enhanced Photocatalytic CO_2 Reduction, ACS Catalysis, 2024, 14, 11617-11625. https://doi.org/10.1021/acscatal.4c01968

[65] Zhang K., Chen H., Wang L., Tang H., Liu Z. Compressive interatomic distance stimulates photocatalytic oxygen-oxygen coupling to hydrogen peroxide, Science Bulletin, 2025, 70, 536-545. https://doi.org/10.1016/j.scib.2024.12.014

[66] Zhu Z., Huang H., Liu L., Chen F., Tian N., Zhang Y., Yu H. Chemically bonded α-Fe_2O_3/Bi_4MO_8Cl dot-on-plate Z-scheme junction with strong internal electric field for selective photo-oxidation of aromatic alcohols, Angewandte Chemie International Edition, 2022, 61, e202203519. https://doi.org/10.1002/anie.202203519

[67] Yu X., Liu X., Wang B., Meng Q., Sun S., Tang Y., Zhao K. An LSPR-based “push-pull” synergetic effect for the enhanced photocatalytic performance of a gold nanorod@cuprous oxide-gold nanoparticle ternary composite, Nanoscale, 2020, 12, 1912-1920. https://doi.org/10.1039/C9NR08808C

[68] Xu Z., Yue W., Li C., Wang L., Xu Y., Ye Z., Zhang J. Rational synthesis of Au-CdS composite photocatalysts for broad-spectrum photocatalytic hydrogen evolution, ACS Nano, 2023, 17, 11655-11664. https://doi.org/10.1021/acsnano.3c02092

[69] Li C., Wu H., Zhu D., Zhou T., Yan M., Chen G., Sun J., Dai G., Ge F., Dong H. High-efficient charge separation driven directionally by pyridine rings grafted on carbon nitride edge for boosting photocatalytic hydrogen evolution, Applied Catalysis B: Environmental, 2021, 297, 120433. https://doi.org/10.1016/j.apcatb.2021.120433